Wang Chih-Ping (Orcid ID: 0000-0003-2393-6808)
Fuselier Stephen A. (Orcid ID: 0000-0003-4101-7901)
Hairston Marc R. (Orcid ID: 0000-0003-4524-4837)
Zhang Xiao-Jia (Orcid ID: 0000-0002-4185-5465)
Zou Shasha (Orcid ID: 0000-0001-7726-2349)
Avanov Levon A. (Orcid ID: 0000-0003-2357-4851)
Strangeway Robert J. (Orcid ID: 0000-0001-9839-1828)
Ahmadi Narges (Orcid ID: 0000-0001-5267-0485)

Author Manuscript

Event studies of O^+ density variability within quiet-time plasma sheet

Chih-Ping Wang[1], Stephen A. Fuselier [2,3], Marc Hairston[4], Xiao-jia Zhang[1,5], Shasha Zou[6], Levon A. Avanov[7], Robert J. Strangeway[5], Narges Ahmadi[8], Jacob Bortnik[1]

1. Department of Atmospheric and Oceanic Sciences, University of California, Los Angeles, California, USA
2. Southwest Research Institute, San Antonio, Texas, USA
3. The University of Texas at San Antonio, San Antonio, Texas, USA
4. William B. Hanson Center for Space Sciences, University of Texas at Dallas, Richardson, Texas, USA
5. Department of Earth, Planetary, and Space Physics, University of California, Los Angeles, California, USA
6. Department of Climate and Space Sciences and Engineering, University of Michigan, Ann Arbor, Michigan, USA
7. Goddard Space Flight Center, NASA, Greenbelt, Maryland, USA
8. LASP, University of Colorado, Boulder, Colorado, USA

This is the author manuscript accepted for publication and has undergone full peer review but has not been through the copyediting, typesetting, pagination and proofreading process, which may lead to differences between this version and the Version of Record. Please cite this article as doi: 10.1029/2019JA026644

This article is protected by copyright. All rights reserved.

Submit to

Journal of Geophysical Research

Author Manuscript

This article is protected by copyright. All rights reserved.

Author Manuscript

Abstract. To understand the variations of the O^+ ions in the quiet-time plasma sheet between the regions of cold-dense plasma sheet (CDPS) and hot plasma sheet (HPS), we conduct three event studies. These studies investigate the O^+ densities in the two regions and how they are correlated with the strength of two magnetospheric sources important to ion outflows: the soft electron flux and Poynting flux toward the ionosphere. The CDPS is characterized by two-components ions (one hot component mixed with one cold component), while the HPS ions consist of only one single hot component. Comparing the O^+ density between the CDPS and HPS of the same event, the average CDPS O^+ density was higher by a factor of ~2-5. Compared to the HPS, the soft electron flux source within the CDPS was higher, consistent with the fact that the soft electron precipitation and O^+ upward number fluxes observed in the ionosphere were also higher within the CDPS. In the plasma sheet, broadband ultra-low-frequency electric and magnetic field waves with the characteristics of kinetic Alfvén waves (KAW) were often more intense within the CDPS, providing a stronger Poynting flux source. In addition, electron resonant interaction with KAW results in acceleration along the magnetic fields, and thus may drive the observed soft electron precipitation. These correlations suggest that the higher soft electron precipitation and Poynting flux coming from the magnetospheric CDPS likely produce larger ionospheric O^+ outflows back to the magnetosphere, thus resulting in the higher O^+ density within the CDPS.

This article is protected by copyright. All rights reserved.

Author Manuscript

This article is protected by copyright. All rights reserved.

Author Manuscript

1. Introduction

H^+ and O^+ ions are the two main ion species in the Earth's plasma sheet. H^+ ions can originate from either the solar wind or the ionosphere, whereas ion outflow from the ionosphere is the sole source for the plasma sheet O^+ ions. The plasma sheet O^+ density is typically smaller than the H^+ density by a factor of ~10 to over 1000. Previous studies of the O^+ density variations (e.g., Lennartsson and Shelley, 1986; Daglis, 2006; Kistler et al., 2006; Mouikis et al., 2010; Keika et al., 2013; Chaston et al., 2014; 2015; Maggiolo and Kistler, 2014; Wang et al., 2016) found that statistically the average plasma sheet O^+ density is higher during disturbed times, for example, during higher Kp and AE, or lower Dst, than during quiet times. For the quiet-time plasma sheet, the O^+ density is higher when the solar EUV radiation is higher, for example, higher F10.7. However, these studies also pointed out that O^+ densities still exhibit a large variation when limiting the ranges of these activity indices.

The plasma sheet can be separated into two plasma regimes based on their ion spectral characteristics. Typically, the plasma sheet ions consist of one single component of a Maxwellian or kappa distribution (e.g., Christon et al., 1989) with the peak energy at several keV. Sometimes, this single component ion plasma sheet is mixed with a second component with a relatively lower peak energy at several hundreds of eV, resulting in a higher density and lower temperature. This two-component ion plasma sheet is referred to as either the mixed region (Fuselier et al., 1999) or the cold and dense plasma sheet (CDPS) (e.g., Baumjohann et al., 1989; Fujimoto et al., 1996; Terasawa et al., 1997; Wing and Newell, 1998; Stenuit et al., 2002;

This article is protected by copyright. All rights reserved.

Øieroset et al., 2005), and is suggested to result from an inward extension of the low-latitude boundary layer. In this paper, we adopt the term of CDPS for the plasma regime with two-component ions, and refer to the plasma sheet regime with a single hot component as hot plasma sheet (HPS). The CDPS is observed most frequently near the flanks, and it extends farther inward during quiet times (e.g., Nishino et al., 2002; Wing and Newell, 2002; Hasegawa et al., 2003; 2004; Wing et al., 2005; Wang et al., 2010). Different mechanisms have been investigated to explain such spatial distributions (e.g., Spence and Kivelson, 1993; Stepanova et al., 2009; Wang et al., 2010). Fuselier et al. (1999) investigated the ion compositions of the HPS and CDPS and showed that the CDPS H^+ density is higher and that the H^+ ions in the low-energy component of the CDPS are the solar wind origin. They showed that the average O^+ densities in these two plasma regimes were roughly the same, but with large variations.

The significant plasma sheet O^+ density variability behind the statistical profiles reported in these previous studies remains to be understood. Such variability should be attributed to the many different factors involved in the complex processes in the ionosphere leading to ion outflow. Two of these factors have a connection to sources within the magnetosphere (e.g., Strangeway 2005; Lotko, 2007): (1) Soft electron (defined here as the electrons with energies $\leq$ ~100 eV) precipitation that enhances ion upflow (or upwelling) in the topside ionosphere (above ~500 km). (2) Poynting flux that provides the electromagnetic energy for wave-ion interaction that accelerates the upflowing ions to outflow ions. Based on previous studies, the strength of these two magnetospheric sources may be different between the CPDS and HPS. Wang et al.

Author Manuscript

This article is protected by copyright. All rights reserved.

(2007) showed that the electron temperature is several hundreds of eV in the HPS and is <~100 eV in the CDPS. Thus, the CDPS is expected to provide stronger soft electron precipitation down to the ionosphere than does the HPS. On the other hand, as the waves driven by the magnetopause disturbances propagated inward from the magnetopause, they may couple more easily to shear Alfvén waves within the CDPS than the HPS because of its stronger spatial gradients of Alfvén speed (e.g, Chaston et al., 2005), thus providing stronger Poynting flux into the ionosphere. Thus, the expected higher strength for these two sources in the CDPS than HPS likely drive stronger O^+ outflow back into the CDPS, if assuming other circumstantial conditions are the same.

The objective of this paper is to revisit the O^+ density variability in the HPS and CDPS and to investigate whether the strength of the above two magnetospheric sources for ion outflow are correlated with the density variability. Since the effect of these two sources, if there is any, was likely washed out in the previous statistical study that included events under wide ranges of geomagnetic activity and solar radiation, here we conduct event studies with a focus on quiet time events only and on comparing the HPS and CDPS observed within the same event. This way we should better limit the variations due to the dependence on the geomagnetic activity and solar radiation. In the plasma sheet, we investigate O^+ density, soft electron flux, and Poynting flux observed by Magnetospheric Multiscale (MMS) spacecraft. In the topside ionosphere, we investigate the soft electron precipitation and O^+ upflow number flux observed by Defense Metrological Satellite Program (DMSP). This paper is organized as follows. The MMS and

Author Manuscript

This article is protected by copyright. All rights reserved.

DMSP data are described in section 2. In section 3, we present three events and our analysis in details. Conclusions of our findings and discussion are given in section 4.

2. Data

For the events presented in this paper, we use MMS observations in the magnetosphere and DMSP measurements in the ionosphere. MMS is a four-spacecraft constellation (Tooley et al., 2016). The spacecraft is at a low inclination orbit (28.5^o) with the apogee of ~25 R_E and the orbital period of ~3 days. Electrons and ions from 10 eV to 30 keV (sample per 4.5 s) are measured by Dual Electron Spectrometers (DES) and Dual Ion Spectrometers (DIS), respectively, of Fast Plasma Investigation (FPI) (Pollock et al., 2016). The H^+ and O^+ ions from 1 eV to 40 keV (sample per 0.625 s) are measured by Hot Plasma Composition Analyzer (HPCA) (Young et al., 2016). The electric and magnetic fields are measured by FIELDS instrument (Torbert et al., 2016) with the magnetic fields (16 samples/s) measured by two flux-gate magnetometers (AFG and DFG) and the electric fields (32 samples/s) measured by Axial and Spin-plane Double-Probe electric-field sensors (ADP and SDP), as well as high frequency (from ~8 to 8000 Hz) waves from Digital Signal Processor (DSP).

The HPCA is a time-of-flight mass spectrometer that measures start-stop coincidences to determine the mass per charge of ions entering the instrument. The O^+ fluxes measured by HPCA can be contaminated by accidental coincidence events when there are very high H^+ fluxes in a high-density region, such as in the magnetosheath, LLBL, or, to a much lesser extent, the CDPS. To reduce these accidental coincidences, HPCA includes a radiofrequency (RF) on the

Author Manuscript

This article is protected by copyright. All rights reserved.

Author Manuscript

electrostatic analyzer that is designed to attenuate intense proton fluxes while transmitting heavier species. The RF applies electric fields with the amplitudes and frequencies tuned so that the faster protons see only a single wave cycle and are deflected, while the heavier and slower O^+ ions experience many electric field oscillations which tend to cancel each other out, so there is only small deflection for the O^+ ions. Different proton attenuation factors are applied on different MMS spacecraft and different energies. For example, for MMS-1 and MMS-2, the RF attenuation results in a proton reduction by a factor of 2 from ~250 eV to 1 keV and a lower reduction factor for protons from ~1 to 4 keV. For MMS-3 and MMS-4, the RF produces a factor of ~10 reduction from 250 eV and 1 keV and a lower reduction factor for protons from ~1 to 4 keV.

We use ion and electron precipitation fluxes, plasma drift flows, and O^+ densities in the ionosphere measured by the DMSP F16 and F18 satellites. The DMSP satellites are in polar Sun-synchronous circular orbits with high inclination (98°) at 840 km altitude and an orbital period of ~101 min. Electron and ion precipitation fluxes from 30 eV to 30 keV (sample per 1 s) are measured by Special Sensor J (SSJ) (Meng and Kroehl, 1977; Hardy et al., 1984). The Special Sensor for Ions Electrons and Scintillation (SSIES) (Rich, 1994) Ion Drift Meter (IDM) (Heelis and Hanson, 1998) measures the drift flows (sample per 1 s) along the two cross-track, orthogonal directions: the horizontal flow, V_y, is positive looking to the left of the orbital plane (positive for sunward flows), and the vertical flow, V_z, is positive in the upward spacecraft zenith direction (positive for upward flows). The O^+ density (sample per 1 s) is obtained by multiplying

This article is protected by copyright. All rights reserved.

the total density by the density ratio of O^+ measured by the Retarding Potential Analyzer (RPA). The measured V_z is adjusted by using the baseline adjustment technique of Redmon et al., (2010). For the solar wind and IMF conditions, we use 1 min OMNI solar wind and IMF data (King and Papitashvili, 2005). The OMNI data have been time shifted to the Earth's bow shock nose from the locations of the solar wind monitors. We also use IMF measured by ARTEMIS when it was in the solar wind.

3. Observations

In this section, we present the analysis of MMS and DMSP observations of the CDPS and HPS for three events. We select these three events because both the MMS and DMSP data had good and reliable quality. Events 1 and 2 were near the dusk flank and event 3 was deep within the central magnetotail at small |Y|.

3.1. Event 1

Figure 1 shows an event near the duskside flank from 00:30 to 02:30 UT on 14 September 2017. During this event, ARTEMIS was in the solar wind at X ~8 and Y ~ –56 R_E and the ARTEMIS IMF was in general consistent with the OMNI IMF. Since ARTEMIS was much closer to the Earth than the solar wind monitors, we show in Figure 1a the IMF measured by ARTEMIS P1 spacecraft. From ~23:10 UT of 13 September 2017 up to this interval, IMF was weakly northward. During this interval in Figure 1, IMF was mostly northward before 02:18 UT, except for a brief excursion to a weakly southward IMF from ~01:50 to 02:00 UT. The solar wind speeds varied from ~330 to 380 km/s. There was an increase in the solar wind density from

Author Manuscript

This article is protected by copyright. All rights reserved.

8 to 20 cm^{-3} and the solar wind dynamic pressure increased from ~1 to 3.5 nPa around 01:10 UT. F10.7 was 75. The geomagnetic condition was relatively quiet with Kp = 2, the highest AE ~80 nT, and the lowest ASYM-H ~ –10 nT. MMS was on the outbound leg of its orbit, moving from (–3.7, 17, –1.5) to (–4.3, 18.3, –2.4) R_E at the speed of 1.3 km/s. The spacecraft trajectory was approximately parallel to the model magnetopause predicted by Shue et al. (1997).

Figure 1 shows that MMS was in the plasma sheet until ~02:18 UT and entered the magnetosheath afterward. The magnetosheath interval, as indicated by the green horizontal bar on the top of Figure 1, is identified by its high density of > 10 cm^{-3}, low ion temperature of ~0.1 keV, and strong tailward flow of ~300 km/s, as shown in Figures 1e, 1f, and 1g, respectively. When within the plasma sheet, MMS observed distinctly the HPS before 01:20 UT and the CDPS from 01:20 UT to 02:18 UT, as indicated by the blue and red horizontal bars on the top of Figure 1, respectively. The single-component feature of the HPS and the two-component feature of CDPS can be visually discernable in the ion energy spectrum in Figures 1c and 1i. The spectrum for two-component ions have either two peaks (like those seen before 01:55 UT) or one broad peak with a plateau (like those seen after 01:55 UT). As done in the previous studies (e.g., Wing and Newell, 1998; Wang et al., 2012), we can further confirm our visual determination by fitting the observed spectrum with either a single or two-component kappa distributions. We determine which fitting is better by comparing the linear correlation coefficients of the fitting. As shown in Figure 1i for the HPS at 00:50 UT (blue solar line) as an example, the single-component feature is confirmed by that the observed spectrum can be well fitted (the linear

Author Manuscript

This article is protected by copyright. All rights reserved.

Author Manuscript

correlation coefficient of the fitting is 0.9) by a single component Kappa distribution (blue dotted line), $f = N_0 \left(\frac{m}{2\pi\kappa E_0}\right)^{3/2} \frac{\Gamma(\kappa+1)}{\Gamma(\kappa-1/2)} \left[1+\frac{E}{\kappa E_0}\right]^{-\kappa-1}$, with κ = 30, N_0 = 0.75 cm^{-3}, and E_0 = 1.5 keV. In comparison, as shown in Figure 1j, the observed CDPS spectrum at 01:42 UT (red solid curve) is well fitted (the linear correlation coefficient of the fitting is 0.98) by a two-component Kappa distribution (blue solid curves), $f = f_h + f_c$. The parameters for the hot component (blue dotted line) in the fitting are κ_h = 4, $N_{0,h}$ = 1 cm^{-3}, and $E_{0,h}$ = 2.5 keV and for the cold component (red dotted line) are κ_c = 5, $N_{0,c}$ = 1.5 cm^{-3}, and $E_{0,c}$ = 0.25 keV. Note that, after 01:55 UT, the two peaks became closer to each other so that the spectrum appeared to have a broad peak with a plateau, our fitting (not shown) confirms that the observed spectrum still consisted of two components. Note that this fitting determination may be less certain for some spectrum, but such situation was relatively infrequent compared to the majority in the three events presented in this study. Comparing the two-components CDPS ions in Figure 1i with the single-component HPS ions and with the single-component magnetosheath ions shows that the CDPS ions are a mixture of the hot HPS ions with the cold ions from the magnetosheath. Both the plasma and magnetic fields within the HPS interval were steady but were more disturbed within the CDPS interval. As shown in Figures 1b, 1e, and 1g, within the CDPS interval, there were several sporadic and transient appearance of the magnetosheath-like plasma, as indicated by the purple triangles on the top of Figure 1. The magnetosheath-like plasma had no hot keV plasma sheet ions. Its density was lower than that of the magnetosheath but higher than that of the CDPS and it had substantial tailward flow. This sporadic appearance of the magnetosheath-like plasma thus suggests that the

This article is protected by copyright. All rights reserved.

magnetopause surface was disturbed and thus the disturbance could provide an energy source for the waves inside the magnetosphere. As for electrons, Figure 1d shows the electron energy fluxes averaged over the parallel and anti-parallel angular ranges. Figures 1f, and 1j show that the electron thermal energy was ~500 eV in the HPS, but dropped to ~100 eV in the CDPS, thus the soft electron fluxes in the CDPS were substantially higher than those in the HPS. The soft electrons in the CDPS are counterstreaming, different from the one-direction feature of the magnetosheath soft electrons. Figure 1h shows the integrated soft electron energy fluxes (integrated over the range of 30 eV to 100 eV) within the angular range in the direction toward the ionosphere. We exclude the magnetosheath and the magnetosheath-like plasma intervals by using the criteria of plasma beta ≥ 1 and $V_x \geq -50$ km/s and by requiring the energy fluxes of the 10 keV ions to be higher than a given value (we use 10^6 eV/(cm^2-s-sr-eV) for this event based on the average fluxes of the HPS). The soft electron fluxes within the CDPS were about an order of magnitude higher than those within the HPS.

In this event, despite the fact that MMS did not observe the CDPS until 01:20 UT, the CDPS was already formed no later than 00:55 UT, as indicated by the DMSP observations shown later. This timing is reasonable since the IMF had been northward for more than 1 hr prior to the start of this event. Spatially, the region of the CDPS was near the magnetopause and the HPS was further inward. MMS was first in the HPS and then encountered the CDPS shortly after the increase of the solar wind dynamic pressure, suggesting that the region of the CDPS was pushed inward to the MMS location as the magnetosphere was compressed.

Author Manuscript

This article is protected by copyright. All rights reserved.

Author Manuscript

Figures 2a and 2b show the RF-corrected energy fluxes of the H^+ and O^+ ions, respectively, from MMS-2 for event 1, and those from MMS-3 are shown in Figures 2c and 2d, respectively. The intervals of the HPS, CDPS, and magnetosheath are indicated by the blue, red, and green bars on the top of Figure 2, and the magnetosheath-like plasma is indicated by the purple triangles. As described in section 2, the H^+ reduction factors produced by the RF correction are lower for MMS-2 than for MMS-3. Figures 2f, 2g, 2h compare the accumulated counts for the H^+ (blue lines) and O^+ ions (red lines) in the HPS, CDPS, and magnetosheath, respectively, measured by MMS-2 (top panels) and MMS-3 (bottom panels). The counts were accumulated within a 3-minute period centered at the times indicated by the vertical dotted lines in Figures 2a-e. Spurious O^+ counts are due to very large H^+ counts so that the energy spectrum and peak energy of the spurious O^+ ions would track those of the H^+ ion. This similarity can be seen in the example of the spectrum shown in Figure 2h for the magnetosheath ions observed by MMS-2. Compared with MMS-2, the higher reduction factor in the H^+ counts in MMS-3 results in fewer spurious O^+ counts. This can be seen in Figure 1h for the MMS-3 that the O^+ spectrum was no longer similar to the H^+ spectrum because of the larger reduction. Thus, we can determine that the O^+ counts are not reliable when there was a clear difference between the counts of MMS-2 and MMS-3. For this event, the O^+ ions within the magnetosheath were not reliable. Within the plasma sheet, the O^+ counts at > ~2 keV were reliable, as indicated by the similar counts observed by MMS-2 and MMS-3. Within the HPS, the O^+ counts at all energies were very low. By comparison, there were more O^+ ions within the CDPS, particularly above 2 keV. Figure 2e

This article is protected by copyright. All rights reserved.

shows the MMS-3 O^+ computed from integrating over the energies > 2 keV (the red dots). For comparison, the densities integrated over all energies, that is, with the unreliable O^+ ions included, are shown by the blue line. The HPS O^+ densities were mostly less than 10^{-3} cm^{-3} with the highest density of $2 \cdot 10^{-3}$ cm^{-3}, while most of the CDPS O^+ densities were greater than 10^{-3} cm^{-3} with the highest density of ~10^{-2} cm^{-3}. The averages of the HPS densities within the 00:30-01:00 UT interval were N_{H^+} = 1.26 cm^{-3} and N_{O^+} = $5.6 \cdot 10^{-4}$ cm^{-3} (N_{O^+}/N_{H^+} = $4.4 \cdot 10^{-4}$), and the averages of the CDPS densities within the 01:30-02:00 UT interval were N_{H^+} = 3.26 cm^{-3} and N_{O^+} = $2.7 \cdot 10^{-3}$ cm^{-3} (N_{O^+}/N_{H^+} = $8.3 \cdot 10^{-4}$). Thus, in this quiet plasma sheet, O^+ density within the region of the CDPS were about a factor of 5 higher than the HPS and the N_{O^+}/N_{H^+} ratio a factor of ~2 higher.

Figure 3 shows the observations of the DMSP F18 over the Northern Hemisphere during event 1. Figure 3a shows that F18 (red line) was at the afternoon MLTs moving dawnward toward higher latitudes. The footprint of the MMS spacecraft, as estimated by using the T96 magnetic field model, was also at the afternoon quadrant. The ion and electron energy spectrum, as shown in Figures 3d and 3e, respectively, show that DMSP first observed the HPS ion and electron precipitation prior to 00:54:55 UT, and then the CDPS from ~00:54:55 to 00:56:20 UT, and afterward the polar-cap, with these three regions indicated by the blue, red, and green horizontal bars on the top of Figure 3d, respectively. The polar-cap is identified by the disappearance of ion precipitation and the existence of the electron polar rain. The distinct single-component feature of the HPS ions and the two-component feature for the CDPS ions can

Author Manuscript

This article is protected by copyright. All rights reserved.

be seen in Figure 3b, qualitatively consistent with their magnetospheric sources observed by MMS shown in Figure 1. Note that this DMSP observation of the CDPS was around 00:55 UT, indicating that the CDPS already existed prior to the MMS encounter of the CDPS at ~01:20 UT. Figure 3c shows that the soft electron precipitation was significantly stronger within the CDPS than within the HPS. Thus, the corresponding integrated soft electron energy fluxes (integrated over the range of 30 to 100 eV), as shown in Figure 3f, were higher (lower) than 10^9 eV/(cm^2-s-sr) in the CDPS (HPS). Figures 3g and 3h show the ionospheric O^+ densities and the N_{O^+}/N ratios, respectively. The high N_{O^+}/N values indicate the O^+ densities were reliable. Figures 3i and 3g shows ionospheric horizontal flows (V_y) and vertical flows (V_z), respectively, and the parameter of $V_z \cdot O^+$ shown in Figure 3k indicates the O^+ fluxes along the vertical direction. Positive V_y is approximately directed toward the Sun, and positive V_z is directed upward. Figure 3g shows the horizontal flows were mainly sunward in the HPS and CDPS and anti-sunward within the polar cap. Figures 3g, 3i, and 3k show that the ionospheric O^+ densities and upward flow speeds were substantially larger, thus stronger upflow O^+ fluxes, within the CDPS than within the HPS. Therefore, the correlations are consistent with that the stronger O^+ upflow seen at the ionospheric end of the CDPS was driven by the more abundant soft electrons coming from the magnetospheric CDPS, and that this stronger O^+ upflow likely plays a role in the O^+ enhancement observed in the magnetospheric CDPS.

Figure 1b shows that the magnetic fields within the CDPS interval were more disturbed than the HPS interval. Figures 4a shows the perturbations of magnetic fields in the 2 perpendicular

Author Manuscript

This article is protected by copyright. All rights reserved.

directions, $\delta B_{\perp x}$ and $\delta B_{\perp y}$, in the mean-field-aligned (MFA) coordinates. The Z_{MFA} is pointed in the direction of the background magnetic field $\mathbf{B}_0$, which is defined in this study as the 5-min running averages of the magnetic fields. The Y_{MFA} ($\perp$y) direction is the cross product of the spacecraft's position unit vector and Z_{MFA}, so that it points azimuthally eastward (the positive Y_{MFA} is pointed eastward), and the X_{MFA} ($\perp$x) direction completes the orthogonal right-hand system (so positive X_{MFA} is pointed outward). The power spectrum of $\delta B_{\perp y}$ within the ULF frequency range is shown in Figure 4b. Broadband ULF magnetic field waves were enhanced within the CDPS, as compared to the HPS. Similarly, as shown in Figures 4c and 4e for electric field perturbations in the perpendicular and parallel directions, respectively, and Figure 4d for the power spectrum of $\delta E_{\perp x}$ fluctuations, broadband ULF electric field waves were also enhanced within the CDPS. Figure 4h compares the medium values of the power spectral density (PSD) of $E_{\perp x}$ and $B_{\perp y}$ within the CDPS interval, the PSD of $E_{\perp x}$ becomes increasingly dominant at frequencies higher than ~1 Hz, indicating the wave become more electrostatic (e.g., Chaston et al., 2013). As shown in Figure 4i the ratio of $E_{\perp x}/B_{\perp y}/V_A$ as a function of frequency, the wave became dispersive at frequencies higher than ~0.2 Hz. This dispersion was consistent with the dispersion of cold plasma kinetic Alfvén wave (KAW) for the KAW dispersion, $E_{\perp x}/B_{\perp y}/V_A = \left(1+k_\perp^2\rho_i^2\right)^{1/2}$ where ρ_i is the ion gyroradius (e.g., Chen and Hasegawa, 1974; Stasiewicz et al., 2000; Johnson and Cheng, 2001; Chaston et al., 2005), as shown by the red line in Figure 4i. The values of V_A = 200 km/s, B = 15 nT, and ion temperature = 5 keV used for the red line are similar

Author Manuscript

This article is protected by copyright. All rights reserved.

to the observed values. These broadband Alfvén waves thus can carry Poynting fluxes down to the ionosphere. Figure 4f shows the power spectrum of Poynting flux parallel to the magnetic field ($\mathbf{S}_{\parallel} = \delta\mathbf{E}\times\delta\mathbf{B}$), and Figure 4g shows the 1 min average of the $\mathbf{S}_{\parallel}$ (excluding the intervals of the magnetosheath-like plasma) with the downward (toward the ionosphere) and upward $|S_{\parallel}|$ shown in red and blue, respectively. The Poynting fluxes within the CDPS were up to two orders of magnitudes higher than within the HPS. Therefore, this stronger Poynting fluxes, together with the larger ionospheric O^+ upflow observed by DMSP, may produce stronger ionospheric O^+ outflow that accounted for the higher O^+ density within the CDPS.

Waves of different modes can contribute to the plasma sheet precipitation, including whistler-mode chorus waves at L shells lower than ~8 and electrostatic electron cyclotron harmonic (ECH) waves at L higher than 8 (e.g., Roeder and Koons, 1989; Zhang et al., 2015), and KAW (e.g., Hasegawa and Mima, 1976, Wygant et al., 2002). Figures 5a and 5b show the magnetic and electric field wave powers near the electron gyro frequencies, and no ECH and whistler-mode chorus waves were observed during this event. Here we evaluate whether the enhanced KAWs within the CDPS shown in Figure 4 are sufficient to cause the soft electron precipitation. The broad spectrum of KAW is produced by the Doppler effect: the observed wave frequency is proportional to the plasma flow speed across the magnetic field. The KAW transverse (relative to the ambient magnetic field) wavelength can be rather small (down to the ion thermal gyroradius), and this means large wavenumber that finally results in large Doppler shift. Therefore, this effect allows us to estimate wave characteristics using the measured

Author Manuscript

This article is protected by copyright. All rights reserved.

Author Manuscript

spectrum. The KAW propagates at about the Alfven speed, and the wave frequency in the plasma reference frame is below the ion cyclotron frequency. Therefore, these waves cannot resonate with electrons through cyclotron resonances, whereas the Landau resonance, with $v_{\|} \approx \omega/k_{\|} \approx v_A$, is only achievable for electrons at very low energies ($m_e v_A^2/2 \sim 1$–2 eV). However, these waves carry parallel electric fields as a result of the hot ion contribution to wave dispersion. The amplitude of the effective scalar potential for these parallel electric fields, Φ, can reach several hundreds of eV, and therefore the resonance width (proportional to $e\Phi$ in the energy space, e.g., Palmadesso (1972)) can be sufficiently large for the resonant interaction with electrons with a wide energy range (e.g., Damiano et al., 2015; Artemyev et al., 2015). To estimate Φ, which determines the range of resonant energies, we need to calculate $E_{\|}/k_{\|}$ that is about $E_{\perp}/k_{\perp}$ for KAW (see more accurate dispersion relation in, e.g. Stasiewicz et al. (2000)). Taking into account that $k_{\perp} \approx \omega/v_{flow}$ for sufficiently small wavelengths (i.e., for $k_{\perp} > 1/\rho_i$, where ρ_i is the ion gyroradius), we estimate $e\Phi$. As shown in Figure 5c, $e\Phi$ is mostly contributed by the low frequency part of the spectrum (corresponding to the most intense wave electric fields), which can reach ~200 eV, i.e., $e\Phi$ is comparable to the electron temperature (see Figure 1e) and almost the entire electron population can resonate with KAWs. When the resonance width ($e\Phi$) is much larger than the resonant energy itself ($\sim m_e v_A^2/2$), the particle velocity change due to a single resonant interaction is controlled by the resonant width, which is about $\Delta v_{||} \sim \sqrt{e\Phi/m_e}$ (e.g., Karimabadi et al. (1990)). Taking into account that the Landau resonance conserves the magnetic moment, $\sim v_{\perp}^2$, we can estimate the pitch-angle change due to one resonant interaction

This article is protected by copyright. All rights reserved.

as $\Delta\alpha \sim \left(\Delta v_{\parallel}/v\right)\sin\alpha \sim \sqrt{e\Phi/T_e}\sin\alpha$, where $T_e = m_e v^2/2/k_B$ is the electron temperature and k_B is the Boltzmann constant. For electrons near the loss-cone, e.g., $\sin\alpha \sim \sin\alpha_{LC}$, we get $\Delta\alpha/\alpha_{LC} \sim \sqrt{e\Phi/T_e}$. Figure 5d shows that this ratio reaches one during intervals with intense KAW waves. Thus, even a single resonant interaction is sufficient to scatter electrons to the loss-cone, i.e., we deal with electron transport to the loss-cone in the way similar to the strong diffusion limit, where the loss-cone is always full. Such intense resonant interactions mean that the precipitating electron flux equals to the electron flux near the loss-cone for all resonant energies, i.e., for the entire electron distribution with energies < T_e. Roughly speaking, intense KAWs expand the loss-cone to the size of $\Delta\alpha$ and fill it with thermal electrons. Therefore, the CDPS soft electron precipitation observed by DMSP at low altitude can be correlated with the CDPS soft electrons observed by MMS through the enhanced KAWs within the CDPS.

3.2. Event 2

In event 1, the regions of the CDPS and HPS were well separated. But this was not always the case. In Figure 6 we investigate event 2 on 11 October 2017 observed by MMS-3, which was also near the duskside flank. Comparing with event 1, the appearance of the CDPS and HPS in event 2 was more sporadic, likely due to the magnetopause being more disturbed. The OMNI data showed that the IMF turned northward at ~01:50 UT and was mostly northward until ~03:50 UT, except for a brief excursion to southward from ~02:15 to 02:27 UT. Within this event, the northward IMF remained around +5 nT from 02:27 to 03:15 UT. The solar wind densities varied between 10 and 15 cm^{-3} and the solar wind dynamic pressure varied between 2.8 and 4.2 nPa.

Author Manuscript

This article is protected by copyright. All rights reserved.

Author Manuscript

F10.7 was 75. Kp was 3 and the lowest SYM-H was –9 nT. AE decreased gradually from ~300 nT at 02:00 UT to the lowest value of 50 nT at 03:30 UT and it then increased back to ~400 nT at 04:20 UT. MMS was on the inbound leg of its orbit, moving from (–5.9, 16.9, 0.9) to (–6.1, 13.7, –0.8) R_E at the speed of 1.5 km/s. Its trajectory was relatively perpendicular the model magnetopause. MMS encountered different plasma regions, as indicated by the bars of different colors on the top of Figure 6. MMS was in the magnetosheath prior to ~02:15 UT, and then encountered intermittently the CDPS and the magnetosheath-like plasma, likely a result of the magnetopause perturbations. MMS entered the magnetosphere at ~02:52 UT and observed intermittent appearance of the CDPS and HPS with intervals dominated by the CDPS or the HPS. The interval of 02:52 to 03:25 UT was dominated by the CDPS, the interval of 03:25 to 04:02 UT was shared by both the CDPS and HPS, and then the interval afterward was dominated by the HPS. As shown in Figures 6b and 6j, the two components of the CDPS were well separated within the CDPS dominated interval but became less so in the latter two intervals with higher HPS dominance. Figure 6f shows that there were no bursty bulk flows within the HPS. In comparison with the HPS dominated interval, the magnetic fields within the CDPS dominated interval were more disturbed as shown in Figure 6a, the electron temperature was below 100 eV as shown in Figure 6e, and the integrated soft electron number fluxes were substantially higher by a factor of up to ~3 as shown in Figure 6g. Figure 6h shows that there were essentially no O^+ ions below ~1 keV in both the CDPS and HPS, and the comparison between the H^+ and O^+ counts shown in Figure 6l indicates that the O^+ fluxes above 1 keV were reliable. The O^+

This article is protected by copyright. All rights reserved.

densities integrated over the energies above 1 keV, as shown in Figure 6i, were clearly higher within the CDPS dominated interval than within the HPS dominated interval. The averages of the HPS densities within the 04:20-04:40 UT interval were N_{H^+} = 2.48 cm^{-3} and N_{O^+} = 0.016 cm^{-3} (N_{O^+}/N_{H^+} = 0.006), and the averages of the CDPS densities within the 03:05-03:25 UT interval were N_{H^+} = 3.49 cm^{-3} and N_{O^+} = 0.03 cm^{-3} (N_{O^+}/N_{H^+} = 0.01). Both the O^+ density and the N_{O^+}/N_{H^+} ratio were about a factor of 2 higher in the CDPS than in the HPS. Comparing with event 1, the O^+ density associated with the CDPS in event 2 was higher. This difference will be discussed in section 4.

Figure 7 shows two DMSP Northern Hemisphere passes over the dayside ionosphere by F-18 (left panels) and F-16 (right panels) during event 2. Figure 7a shows that for both passes, DMSP was moving dawnward from lower latitudes toward higher latitudes. The footprints of the MMS spacecraft were within the afternoon quadrant. Figure 7b shows that during the F-18 pass, DMSP first observed the HPS, then the CDPS between ~02:03:00 to 02:04:10 UT, and afterward the polar cap, as indicated by the blue, red, and green horizontal bars on the top of Figure 7b, respectively. Figure 7d shows that the soft electron precipitation energy fluxes were the most intense within the CDPS, as compared to the other two regions. As shown in Figure 7e, 7h, and 7i, compared with the HPS, the ionospheric O^+ densities, upward flow speeds, and O^+ upward number fluxes were substantially larger within the CDPS. During the F-16 pass, DMSP encountered the HPS, CDPS, and the open LLBL. The open LLBL is identified by the very high fluxes in both low-energy ions and electrons, and the corresponding anti-sunward flows suggest

Author Manuscript

This article is protected by copyright. All rights reserved.

that the magnetic field lines in the LLBL were open. The soft electron precipitation energy fluxes, the ionospheric O^+ densities, upward flow speeds, and upward O^+ fluxes within the CDPS were as strong as those within the open LLBL and were substantially larger than those within the HPS. The peak magnitudes of the upward O^+ fluxes within the CDPS in event 2 were similar to those of event 1.

Figures 8a to 8e show the magnetic and electric field perturbations and their power spectrum for event 2. The different intervals with different CDPS dominance identified above are indicated on the top of Figure 8, and the broadband ULF waves were more enhanced within both the CDPS dominated and HPS dominated intervals than the other two intervals, so do the resulting Poynting fluxes. The peak magnitudes of the Poynting fluxes within the CDPS in event 2 were similar to those in event 1. Figures 8h and 8i indicate that the broadband ULF waves were KAWs. The intense KAWs within the CDPS were sufficient to scatter the soft electrons into the loss cone. No ECH and whistler-mode chorus waves were observed during this event. In comparison, the Poynting fluxes within the HPS dominated interval were as strong as those within the CDPS dominated interval. This suggests that, for this event, the stronger soft electron precipitation from the CDPS might contribute more than do the Poynting fluxes to the more abundant O^+ ions observed within the CDPS in the magnetosphere. In section 4, we will compare the above two duskside flank events.

3.3. Event 3

It has been reported that the CDPS can extend further inward from the flanks under

This article is protected by copyright. All rights reserved.

Author Manuscript

prolonged northward IMF conditions (e.g. Nishino et al., 2002). Here we investigate an event of the CDPS in the central plasma sheet and the associated O^+ density variations on 4 August 2017. Figure 9 shows the observations by MMS-3 during the event at X ~ –22 and Y ~7 R_E. The IMF was strongly northward for ~8 hr from ~23 UT on 3 August 2017 to ~07:00 UT on 4 August 2017. MMS was within the plasma sheet from ~02:00 to 07:30 UT. During this interval, IMF B_z was strong at > +10 nT from ~02:00 to 06:00 UT and reached as high as +20 nT around 03:20 UT. The solar wind density varied significantly between ~15 to 40 cm^{-3} prior to 05:10 UT and were < 20 cm^{-3} after 06:00 UT (there was a data gap in the OMNI data between 05:10 and 06:00 UT), while the solar wind speeds gradually increased from ~400 to 460 km/s. The solar wind dynamic pressure varied strongly between ~4 to 14 nPa before 05:10 UT and was between 4 to 8 nPa after 06:00 UT. F10.7 was 76. SYM-H varied within +10 and +50 nT and Kp increased from 2 to 3. AE remained low with the highest AE of ~150 nT. MMS was near apogee moving from (–22.6, 9.7, 4.3) to (–22.0, 8.8, 2.7) R_E at the speed of 0.34 km/s. As indicated on the top of Figure 9, MMS observed the CDPS prior to ~07:05 UT and the HPS afterward, before MMS encountered the plasma sheet boundary layer at ~07:30 UT then entered the lobe. The RF-correction was not switched on for this event because normally the H^+ fluxes in the tail are too low to cause significant contamination to the other ion species. The O^+ counts in this event were very high and the O^+ fluxes above ~200 eV were reliable, as shown in Figure 9l. As indicated by the O^+ densities integrated over the energies above 200 eV shown in Figure 9i, the O^+ densities were higher within the CDPS than with the HPS. The averages of the HPS densities within the

Author Manuscript

This article is protected by copyright. All rights reserved.

07:10-07:30 UT interval were N_H^+ = 2.36 cm^{-3} and N_O^+ = 0.013 cm^{-3} ($N_O^+/N_H^+ = 6{\cdot}10^{-3}$), and the averages of the CDPS densities within the 05:00-05:20 UT interval (around the maximum O^+ density) were N_H^+ = 3.55 cm^{-3} and N_O^+ = 0.057 cm^{-3} (N_O^+/N_H^+ = 0.02). The CDPS N_O^+/N_H^+ in this event was higher than those in events 1 and 2. Compared with the HPS, the O^+ density in the CDPS was a factor of up to ~4.4 higher and the N_O^+/N_H^+ ratio a factor of up to 3.2 higher. As shown in Figure 9g, the soft electron number fluxes within the CDPS were a factor of ~3 higher than those within the HPS. The electric and magnetic field ULF waves had the characteristics of KAWs. As shown in Figure 9b, the Poynting fluxes within the HPS were not lower than those within the CDPS. In fact, there were a few very strong Poynting flux spikes within the HPS that, as shown in Figure 9f, corresponded to strong plasma flows associated with the field-aligned flows of the plasma sheet boundary layer and perpendicular flows of bursty bulk flows. Within the CDPS interval, the Poynting fluxes and soft electron fluxes after 05:30 UT appeared to be relatively lower than those prior, and the O^+ densities were also found to be lower. Comparing with events 1 and 2, peak soft electron fluxes within the CDPS in this event where higher but peak Poynting fluxes were lower.

Figure 10 shows a DMSP F-18 Southern Hemisphere pass over the nightside ionosphere during event 3. DMSP was moving duskward at the pre-midnight MLTs toward lower latitudes around 23 MLT. The footprint of the MMS spacecraft was within the pre-midnight quadrant. As indicated on the top of Figure 10b, DMSP observed first the CDPS and the HPS, consistent with the MMS observations of the CDPS deep within the central magnetotail. In the tail, ECH and

Author Manuscript

This article is protected by copyright. All rights reserved.

whistler-mode chorus waves were not observed by MMS (not shown), but the amplitudes of the enhanced KAWs were found to be sufficient to explain the soft electron precipitation. Compared with the HPS at lower latitudes, the soft electron precipitation energy fluxes and the ionospheric O^+ density within the CDPS were higher. There were several enhancements in the upward flow speeds within the CDPS, resulting in enhanced O^+ upflow fluxes. The magnitudes of peak O^+ upflow fluxes in this event were similar to those of events 1 and 2.

4. Conclusion and Discussion

We analyze three events observed by MMS in the magnetosphere and DMSP in the topside of the ionosphere to investigate the differences in the plasma sheet O^+ densities between the CDPS and HPS during relatively quiet times, and how the differences correlate with the strength of two magnetospheric sources: the soft electron flux and Poynting flux toward the ionosphere. The three events include two events near the duskside flank and one deep within the central magnetotail. The CDPS is characterized by its two-component ions with one hot component mixed one cold component, while the HPS ions consist of only one single hot component. Comparing the CDPS with the HPS within the same event, we found that the O^+ densities within the CDPS were a factor of ~2 to 5 higher. The CDPS electrons were colder than those in HPS so that the corresponding soft electron number fluxes were higher. In the ionosphere, the soft electron precipitation number fluxes, ion upward flow speeds, and the O^+ upward number fluxes were substantially higher within the CDPS than within the HPS. In the plasma sheet, broadband ULF electric and magnetic field wave power were stronger within the CDPS, and the waves

Author Manuscript

This article is protected by copyright. All rights reserved.

showed the characteristics of kinetic Alfvén waves. As a result, field-aligned Poynting fluxes within the CDPS were higher. From these correlations, we reason that the more intense soft electron precipitation and Poynting fluxes coming from the magnetospheric CDPS likely produce stronger ionospheric O^+ outflow and can thus plausibly explain the higher O^+ densities within the CDPS.

Our finding of the correlations of O^+ density with the strength of the soft electron and Poynting flux sources within the same event partially explains the O^+ variability shown in the previous statistical study of the CDPS and HPS (Fuselier et al., 1999). However, when comparing the CDPS observed in two different events, the difference in the O^+ densities were not correlated with the difference in the strength of the two sources. For example, the CDPS O^+ density in event 2 was about an order of magnitude higher than that of event 1. But the soft electron number fluxes were similar in these two events and the Poynting flux in event 2 was only about a factor of 2 higher. In fact, the HPS O^+ density in event 2 was also an order of magnitude higher than the HPS in event 1. These differences indicate that the baselines for the O^+ densities were different in these two events. We suggest that one possible factor for this baseline difference may be their different magnetospheric pre-conditions. The magnetosphere for event 1 had been quieter, as indicated by the fact that AE* (the maximum AE within the previous 3 hr interval) was 40 nT for event 1 but was ~500 nT in event 2. This pre-condition difference can be seen in that the hot component in event 2 was hotter. Thus, it is likely that O^+ density was greatly enhanced during the high AE period prior to event 2 and populated the plasma sheet. As

Author Manuscript

This article is protected by copyright. All rights reserved.

the IMF turned northward and convection flow became stagnant, this dense O^+ population was not depleted quickly (e.g., Kistler et al., 2006) and thus may linger into the quiet interval of event 2.

Since statistically the occurrence of the CDPS is higher toward the flanks and the width of the CDPS is wider during quiet times than during disturbed times, our findings suggest that the CDPS may contribute to the statistical Y profile of O^+ density from the ISEE data reported by Lennartsson and Shelley (1986), which showed that, for the low AE limit (< 200 nT), the O^+ density is higher toward the flanks. Their results, however, showed that the densities decreased again outside $|Y| = 10\ R_E$. But this may be contributed by a fact that there were much fewer data points outside $|Y| = 10\ R_E$. In other previous statistical studies, Mouikis et al. (2010) established the O^+ spatial distributions from 5 years of Cluster data. However, they only considered densities less than 2 cm^{-3} and therefore excluded most of the CDPS. Wang et al. (2016) used 12 years of Cluster data and did not impose an upper density threshold, and their results showed high O^+ density regions outside $|Y| = 15\ R_E$ closer to the dusk and dawn flanks However, their cross-tail profile was obtained by including all the data regardless the geomagnetic activity. Therefore, future statistical studies with more careful data selection criteria are needed to evaluate the contribution of the CDPS in the spatial distributions of O^+ density.

The statistical study of Dst (Lavraud et al., 2006) showed that the colder and denser plasma sheet built up during a northward IMF pre-storm period can lead to a stronger ring current, than does a less dense pre-storm southward IMF plasma sheet. Event and statistical studies showed

Author Manuscript

This article is protected by copyright. All rights reserved.

Author Manuscript

that the CDPS extends deeper from the flanks to smaller |Y| when the northward IMF is prolonged longer (Wing and Newell, 2002; Nishino et al., 2007; Wang et al., 2010). Our finding of the O^+ ion enhancement associated with the CDPS in this study, including the one with the CDPS deep within the central plasma sheet, thus suggests such O^+ ion increase during the quiet time before a storm may be important to the development of the storm-time ring current.

Acknowledgements

We thank Yun-Ju Chen at University of Texas, Dallas and John Wygant at University of Minnesota for helpful discussion. The work by C.-P. Wang is supported by AFOSR FY2016 MURI and NASA 80NSSC17K0056. Research at Southwest Research Institute was funded by NASA through the MMS contract. The MMS data are available via MMS Science Data Center (https://lasp.colorado.edu/mms/sdc/public/about/how-to/) and SPEDAS. The DMSP data are available for free from Madrigal3 CEDAR Database (http://cedar.openmadrigal.org/). The geomagnetic indices, AE, Kp, and SYM-H are provided by World Data Center C2 for Geomagnetism in Kyoto. We thank J.H. King, N. Papatashvilli at AdnetSystems, and NASA GSFC and CDAWeb for providing the OMNI data.

References

Artemyev, A. V., R. Rankin, and M. Blanco (2015), Electron trapping and acceleration by kinetic Alfven waves in the inner magneto- sphere, *J. Geophys. Res. Space Physics, 120,* 10,305–10,316, doi:10.1002/2015JA021781.

This article is protected by copyright. All rights reserved.

Author Manuscript

Baumjohann, W., G. Paschmann, C.A. Cattell (1989), Average plasma properties in the central plasma sheet. J. Geophys. Res. **94**, 6597.

Chaston, C. C., et al. (2005), Energy deposition by Alfve´n waves into the dayside auroral oval: Cluster and FAST observations, J. Geophys. Res., 110, A02211, doi:10.1029/2004JA010483.

Chaston, C. C., Y. Yao, N. Lin, C. Salem, and G. Ueno (2013), Ion heating by broadband electromagnetic waves in the magnetosheath and across the magnetopause, J. Geophys. Res. Space Physics, 118, 5579–5591, doi:10.1002/jgra.50506.

Chaston, C. C., J. W. Bonnell, J. R. Wygant, C. A. Kletzing, G. D. Reeves, A. Gerrard, L. Lanzerotti, and C. W. Smith (2015), Extreme ionospheric ion energization and electron heating in Alfvén waves in the storm time inner magnetosphere, Geophys. Res. Lett., 42, 10,531–10,540, doi:10.1002/2015GL066674.

Chaston, C. C., J. W. Bonnell,G. D. Reeves, and R. M. Skoug (2016), Driving ionospheric outflows and magnetospheric O^+ energy density with Alfvén waves, Geophys. Res. Lett., 43, 4825–4833, doi:10.1002/2016GL069008.

Chen, L. and A. Hasegawa (1974), Plasma heating by spatial resonance of Alfvén wave, Phys. Fluids, 17, 1399.

Christon, S. P. (1987), A comparison of the Mercury and Earth magnetospheres: Electron measurements and substorm time scales, Icarus, 71, 448–471, *doi:*10.1016/0019-1035(87)90040-6.

This article is protected by copyright. All rights reserved.

Author Manuscript

Daglis, I. A. (2006), Ring Current Dynamics, Space Science Reviews, 10.1007/s11214-006-9104-z, 124, 1-4, (183-202).

Damiano, P. A., J. R. Johnson, and C. C. Chaston (2016), Ion gyrora- dius effects on particle trapping in kinetic Alfvén waves along auroral field lines, *J. Geophys. Res. Space Physics*, *121*, 10,831–10,844, doi:10.1002/2016JA022566.

Fujimoto, M., et al. (1996), Plasma entry from the flanks of the near-Earth magnetotail: GEOTAIL observations in the dawnside-LLBL and the plasma sheet, J. Geoelectr. Geomag., 48, 711.

Fuselier, S. A., R. C. Elphic, *and* J. T. Gosling (1999), Composition measurements in the dusk flank magnetosphere, J. Geophys. Res., 104, 4515–4522, *doi:*10.1029/1998JA900.137.

Karimabadi, H., K. Akimoto, N. Omidi, *and* C. R. Menyuk (1990), Particle acceleration by a wave in a strong magnetic field—Regular and stochastic motion, Phys. Fluids B, 2, 606–628, *doi:*10.1063/1.859296.

Hasegawa, A., and K. Mima (1976), Exact solitary Alfvén wave, *Phys. Rev. Lett.*, *37*, 690–693, doi:10.1103/PhysRevLett.37.690.

Hasegawa, H., M. Fujimoto, K. Maezawa, Y. Saito, T. Mukai (2003), Geotail observations of the dayside outer boundary region: interplanetary magnetic field control and dawn-dusk asymmetry. J. Geophys. Res. 108(A4), 1163. doi:10.1029/2002JA009667

This article is protected by copyright. All rights reserved.

Author Manuscript

Hasegawa, H., M. Fujimoto, Y. Saito, T. Mukai (2004), Dense and stagnant ions in the low-latitude boundary region under northward interplanetary magnetic field. Geophys. Res. Lett. 31, L06802. doi:10.1029/2003GL19120.

Hardy, D. A., L. K. Schmitt, M. S. Gussenhoven, F. J. Marshall, H. C. Yeh, T. L. Shumaker, A. Hube, and J. Pantazis (1984), Precipitating electron and ion detectors (SSJ/4) for the block 5D/flights 6 – 10 DMSP satellites: Calibration and data presentation, Rep. AFGL-TR-84-0317, Air Force Geophys. Lab., Hanscom Air Force Base, Bedford, Mass.

Heelis, R. A., and W. B. Hanson (1998), Measurements of thermal ion drift velocity and temperature using planar sensors, in *Measurement Techniques in Space Plasmas: Particles*, Geophys. Monogr. Ser., vol. **102**, edited by R. F. Pfaff, J. E. Borovsky, and D. T. Young, pp. 61–71, AGU, Washington, D. C.

Johnson, J. R., C.Z. Cheng (2001), Stochastic ion heating at the magnetopause due to kinetic Alfvén waves. Geophys. Res. Lett. 28, 4421–4424.

Keika, K., L. M. Kistler, and P. C. Brandt (2013), Energization of O^+ ions in the Earth's inner magnetosphere and the effects on ring current buildup: A review of previous observations and possible mechanisms, J. Geophys. Res. Space Physics, 118, 4441–4464, doi:10.1002/jgra.50371.

King, J. H., and N. E. Papitashvili (2005), Solar wind spatial scales in and comparisons of hourly Wind and ACE plasma and magnetic field data, J. Geophys. Res., 110, A02104, doi:10.1029/2004JA010649.

This article is protected by copyright. All rights reserved.

Author Manuscript

Kistler, L. M., et al. (2006), Ion composition and pressure changes in storm time and nonstorm substorms in the vicinity of the near-Earth neutral line, J. Geophys. Res., 111, A11222, doi:10.1029/2006JA011939.

Lavraud, B., M. F. Thomsen, J. E. Borovsky, M. H. Denten, and T. I. Pulkkinen (2006), Magnetosphere preconditioning under northward IMF: Evidence from the study of coronal mass ejection and corotating interaction region geoeffectiveness, J. Geophys. Res., 111, A09208, doi:10.1029/ 2005JA011566.

Lennartsson, W., and E. G. Shelley (1986), Survey of 0.1- to 16-keV/e plasma sheet ion composition, J. Geophys. Res., 91, 3061–3076, doi:10.1029/JA091iA03p03061.

Lotko, W. (2007), The magnetosphere-ionosphere system from the perspec- tive of plasma circulation: A tutorial, J. Atmos. Sol. Terr. Phys., 69(3), 191–211, doi:10.1016/j.jastp.2006.08.011.

Maggiolo, R., and L. M. Kistler (2014), Spatial variation in the plasma sheet composition: Dependence on geomag- netic and solar activity, J. Geophys. Res. Space Physics, 119, 2836–2857, doi:10.1002/2013JA019517.

Meng, C.-I., and H. Kroehl (1977), Intense uniform precipitation of low-energy electrons over the polar cap, J. Geophys. Res., 82(16), 2305–2313, doi:10.1029/JA082i016p02305.

Mouikis, C. G., L. M. Kistler, Y. H. Liu, B. Klecker, A. Korth, and I. Dandouras (2010), H + and O + content of the plasma sheet at 15–19 Re as a function of geomagnetic and solar activity,

This article is protected by copyright. All rights reserved.

J. Geophys. Res., 115, A00J16, doi:10.1029/2010JA015978.

Pollock, C., Moore, T., Jacques, A., Burch, J., Gliese, U., Saito, Y., et al. (2016). Fast plasma investigation for magnetospheric multiscale.Space Science Reviews, 199(1–4), 331–406. https://doi.org/10.1007/s11214-016-0245-4

Nishino, M. N., T. Terasawa, *and* M. Hoshino (2002), Increase of the tail plasma content during the northward interplanetary magnetic field intervals: Case studies, J. Geophys. Res., 107*(*A9*), 1261, doi:*10.1029/2002JA009268.

Nishino, M. N., Fujimoto, M., Ueno, G., Maezawa, K., Mukai, T., & Saito, Y. (2007). Geotail observations of two-component protons in the midnight plasma sheet. Annales Geophysicae, 25*(*10*),* 2229–2245. https://doi.org/10.5194/angeo-25-2229-2007

Øieroset, M., J. Raeder, T. D. Phan, S. Wing, J. P. McFadden, W. Li, M. Fujimoto, H. Re`me, and A. Balogh (2005), Global cooling and densification of the plasma sheet during an extended period of purely northward IMF on October 22 – 24, 2003, Geophys. Res. Lettl., 32, L12S07, doi:10.1029/2004GL021523.

Palmadesso, P. J. (1972), Resonance, particle trapping, and Landau damping in finite amplitude obliquely propagating waves, Phys. Fluids, 15, 2006–2013, *doi:*10.1063/1.1693815.

Redmon, R. J., W. K. Peterson, L. Andersson, E. A. Kihn, W. F. Denig, M. Hairston, and R. Coley (2010), Vertical thermal O^+ flows at 850 km in dynamic auroral boundary coordinates, J. Geophys. Res., 115, A00J08, doi:10.1029/2010JA015589.

Author Manuscript

This article is protected by copyright. All rights reserved.

Author Manuscript

Rich, F. J. (1994), Users Guide for the Topside Ionospheric Plasma Monitor (SSIES, SSIES-2, and SSIES-3) on Spacecraft of the Defense Meteorological Satellite Program (DMSP). Volume I: Technical Description, Phillips Laboratory Technical Report PL-TR-94-2187,

Roeder, J. L., and H. C. Koons (1989), A survey of electron cyclotron waves in the magnetosphere and the diffuse auroral electron precipitation, J. Geophys. Res., 94(A3), 2529–2541.

Shue, J.-H., J. K. Chao, H. C. Fu, C. T. Russell, P. Song, K. K. Khurana, *and* H. J. Singer (1997), A new functional form to study the solar wind control of the magnetopause size and shape, J. Geophys. Res., 102, 9497–9511, *doi:*10.1029/97JA00196.

Spence, H. E., and M. G. Kivelson (1993), Contributions of the low- latitude boundary layer to the finite width magnetotail convection model, J. Geophys. Res., 98, 15,487−15,496, doi:10.1029/93JA01531.

Stasiewicz, K., et al. (2000), Small scale Alfvénic structure in the aurora, Space Sci. Rev., 92, 423.

Stenuit, H., M. Fujimoto, S.A. Fuselier, J.-A. Sauvaud, S. Wing, A. Fedorov, E. Budnik, S.P. Savin, K.J. Trattner, V. Angelopoulos, J. Bonnel, T.D. Phan, T. Mukai, A. Pedersen (2002), Multi-spacecraft study ion the dynamics of the dusk-flank magnetosphere under northward IMF: January 10–11, 1997. J. Geophys. Res. 107(A10), 1333. doi:10.1029/2002JA9009246

This article is protected by copyright. All rights reserved.

Author Manuscript

Stepanova, M., E. E. Antonova, D. Paredes-Davis, I. L. Ovchinnikov, and Y. I. Yermolaev (2009), Spatial variation of eddy-diffusion coefficients in the turbulent plasma sheet during substorms, Ann. Geophys., 27, 1407–1411.

Strangeway, R. J., R. E. Ergun, Y.-J. Su, C. W. Carlson, and R. C. Elphic (2005), Factors controlling ionospheric outflows as observed at intermediate altitudes, J. Geophys. Res., 110, A03221, doi:10.1029/2004JA010829.

Terasawa, T., et al. (1997), Solar wind control of density and temperature in the near-Earth plasma sheet: WIND/GEOTAIL collaboration, Geophys. Res. Lett., 24(8), 935–938, doi:10.1029/96GL04018.

Tooley, C. R., R. K. Black, B. P. Robertson, J. M. Stone, S. E. Pope, and G. T. Davis (2014), The Magnetospheric Multiscale constellation, Space Sci. Rev., doi:10.1007/s11214-015-0220-5.

Torbert, R. B., Russell, C. T., Magnes, W., Ergun, R. E., Lindqvist, P.-A., LeContel, O., et al. (2016). The FIELDS instrument suite on MMS: Scientific objectives, measurements, and data products. Space Science Reviews, 199(1-4), 105–135. https://doi.org/10.1007/s11214-014-0109-8

Wang, C.-P., L. R. Lyons, T. Nagai, J. M. Weygand, and R. W. McEntire (2007), Sources, transport, and distributions of plasma sheet ions and electrons and dependences on interplanetary parameters under northward interplanetary magnetic field, J. Geophys. Res., 112, A10224, doi:10.1029/2007JA012522.

This article is protected by copyright. All rights reserved.

Author Manuscript

Wang, C.-P., L. R. Lyons, T. Nagai, J. M. Weygand, and A. T. Y. Lui (2010), Evolution of plasma sheet particle content under different interplanetary magnetic field conditions, J. Geophys. Res., 115, A06210, doi:10.1029/2009JA015028.

Wang, C.-P., M. Gkioulidou, L. R. Lyons, and V. Angelopoulos (2012), Spatial distributions of the ion to electron temperature ratio in the magnetosheath and plasma sheet, J. Geophys. Res., 117, A08215, doi:10.1029/2012JA017658.

Wang, Jing, Jinbin Cao and Wenlong Liu, Distribution of hydrogen and oxygen ion species in the plasmasheet, *Advances in Space Research*, 10.1016/j.asr.2016.04.008, **58**, 1, (84-91), (2016).

Wing, S., P.T. Newell (1998), Central plasma sheet ion properties as inferred from ionospheric observations. J. Geo- phys. Res. 103, 6785–6800.

Wing, S., and P. T. Newell (2002), 2D plasma sheet ion density and tem- perature profiles for northward and southward IMF, Geophys. Res. Lett., 29(9), 1307, doi:10.1029/2001GL013950.

Wing, S., J. R. Johnson, P. T. Newell, and C.-I. Meng (2005), Dawn-dusk asymmetries, ion spectra, and sources in the northward interplanetary magnetic field plasma sheet, J. Geophys. Res., 110, A08205, doi:10.1029/2005JA011086.

Wygant, J. R., et al. (2002), Evidence for kinetic Alfvén waves and parallel electron energization at 4–6 R_E altitudes in the plasma sheet boundary layer, *J. Geophys. Res.*, *107*, 1201, doi:10.1029/2001JA900113.

This article is protected by copyright. All rights reserved.

Young, D. T., Burch, J. L, Gomez, R. G., De Los Santos, A., Miller, G. P., Wilson, P., et al. (2016). Hot plasma composition analyzer for the Magnetospheric Multiscale mission. Space Science Reviews, 199, 407–470. https://doi.org/10.1007/s11214-014-0119-6

Zhang, X.-J., V. Angelopoulos, B. Ni, and R. M. Thorne (2015), Predominance of ECH wave contribution to diffuse aurora in Earth's outer magnetosphere, J. Geophys. Res. Space Physics, 120, 295–309, doi:10.1002/2014JA020455.

Author Manuscript

This article is protected by copyright. All rights reserved.

Author Manuscript

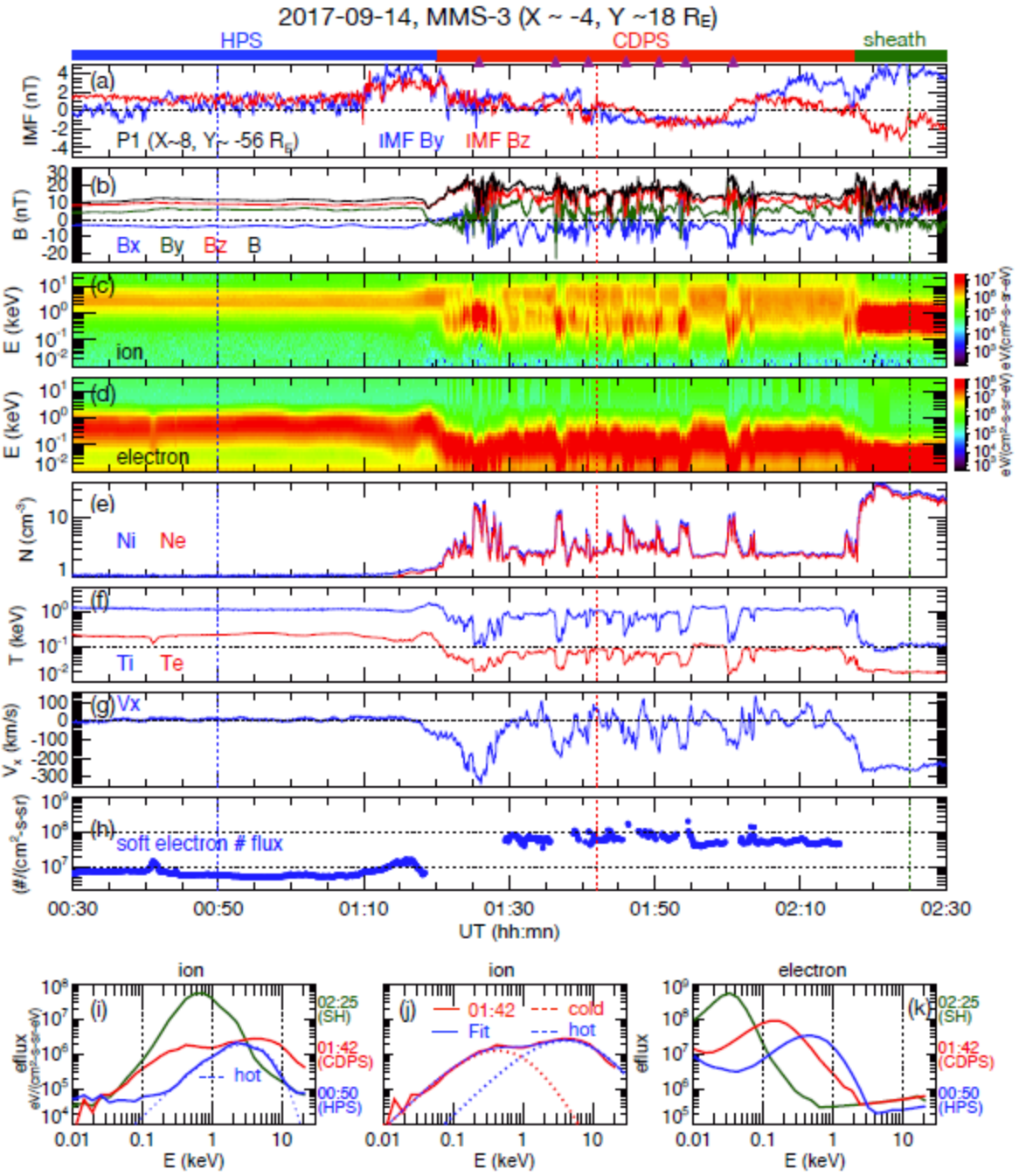

Figure 1. Event 1 on 14 September 2017. (a) IMF from ARTEMIS. The MMS-3 observations of (b) magnetic fields, (c) ion energy fluxes, (d) electron energy fluxes, (e) ion and electron number

This article is protected by copyright. All rights reserved.

densities, (f) ion and electron temperatures, (g) ion bulk flow in the X_{GSM} direction, (h) electron number fluxes integrated from 30 to 100 eV. Energy spectrum of (i) ion and (k) electron energy fluxes at three different times indicated by the vertical dotted lines in Figures 1a to 1h. The blue dotted line in (i) is the fit to the HPS. (j) Observed and fit ion energy fluxes at 01:42 UT.

Author Manuscript

This article is protected by copyright. All rights reserved.

Author Manuscript

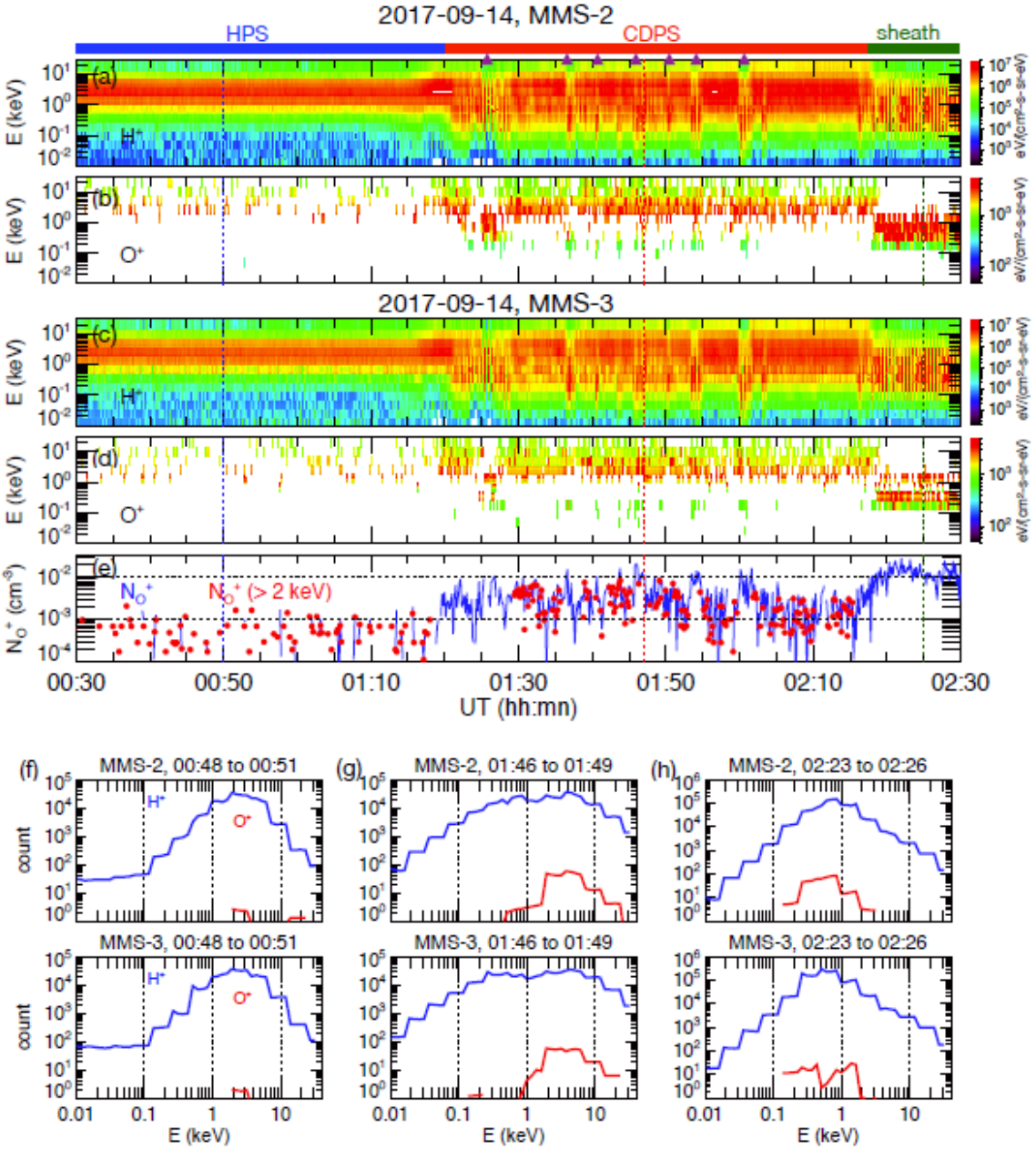

Figure 2. Event 1 on 14 September 2017. (a) H^+ and (b) O^+ energy fluxes observed by MMS-2. (c) H^+ and (d) O^+ energy fluxes observed by MMS-3. (e) the O^+ densities integrated over all energies (blue line) and over the energies > 2 keV (red dots) observed by MMS-3. (f)-(h) The accumulated H^+ (blue curves) and O^+ (red curves) counts observed by MMS-2 (top) and MMS-3

This article is protected by copyright. All rights reserved.

(bottom) within the 3-min intervals (indicated on the top of each plot) at the three different times indicated by the vertical dotted lines in Figures 2a-2e.

Author Manuscript

This article is protected by copyright. All rights reserved.

Author Manuscript

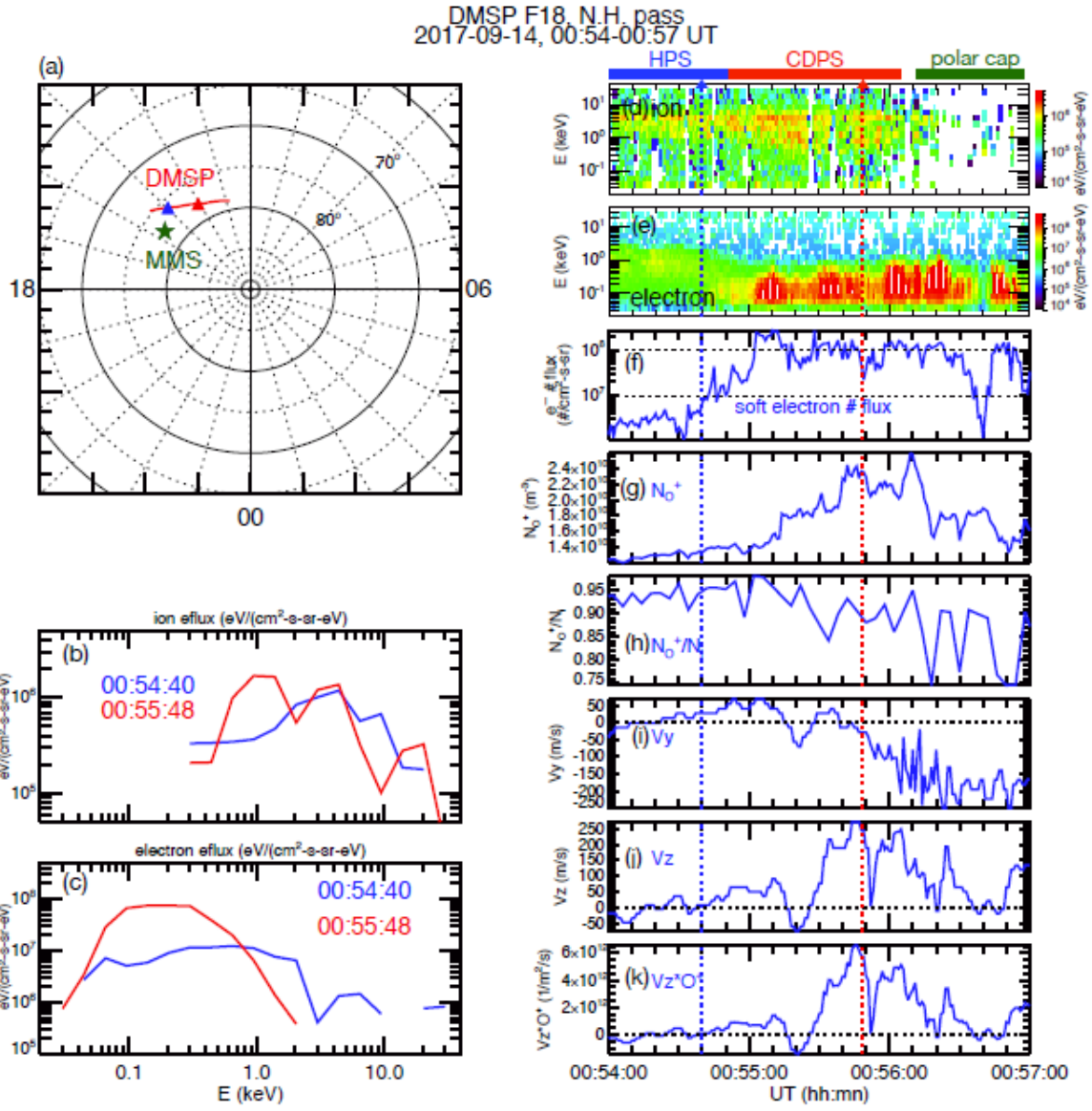

Figure 3. DMSP F-18 observations from 00:54 to 00:57 UT on 14 September 2017 for event 1. (a) The red line indicates the DMSP trajectory (the red and blue triangles indicate the location corresponding to the two different times indicated by the vertical dotted lines in Figures 3d-3k.). The green star indicates the footprint of the MMS spacecraft. Energy spectrum of (b) ion and (c) electron energy fluxes at the two different times. Temporal profiles of (d) ion and (e) electron

This article is protected by copyright. All rights reserved.

energy fluxes, (f) electron number fluxes integrated over 30 to 100 eV, (g) the O^+ densities, (h) O^+/ion density ratios, (i) sunward flows, (j) upward flows, and (k) the O^+ upward fluxes.

Author Manuscript

This article is protected by copyright. All rights reserved.

Author Manuscript

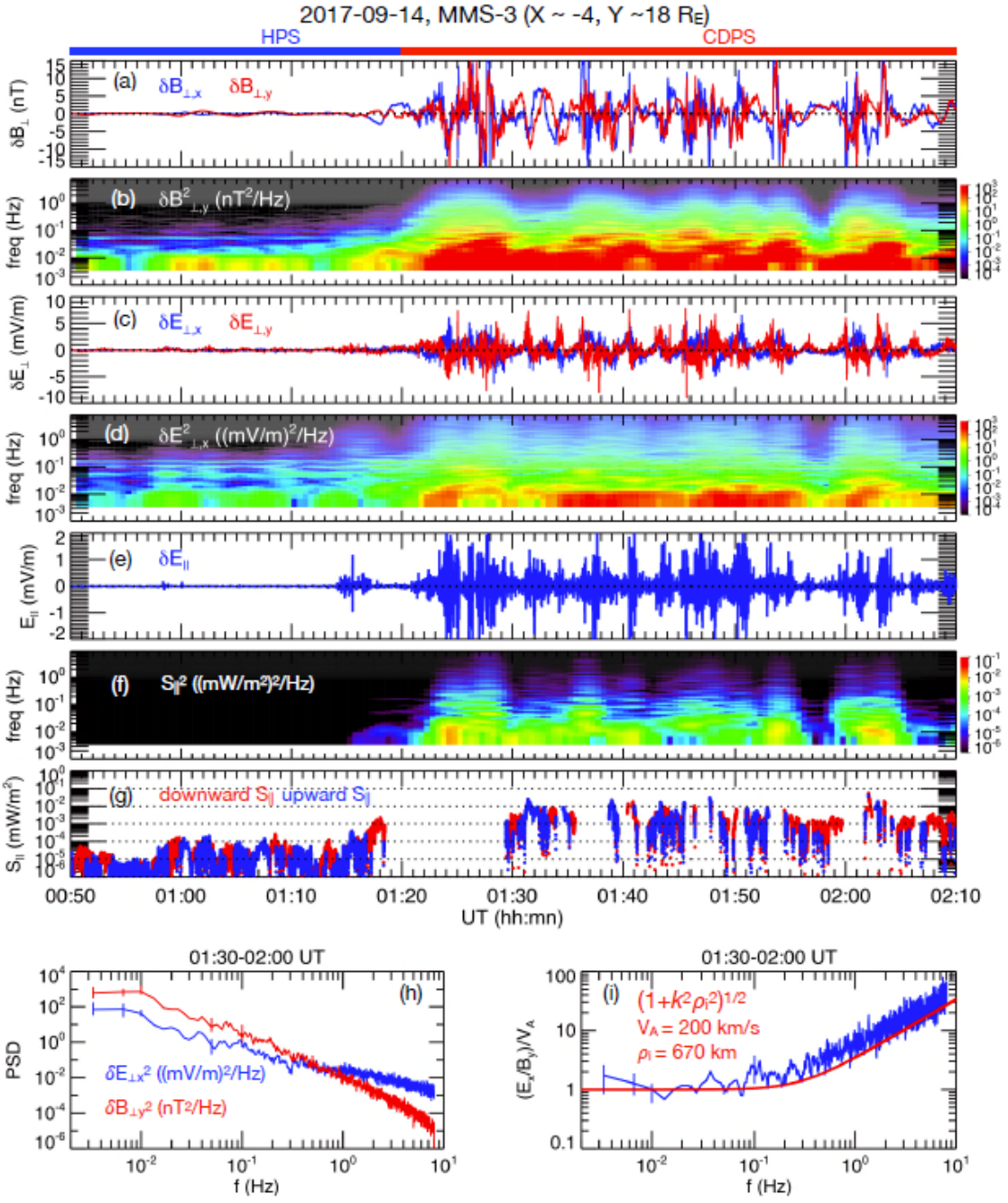

Figure 4. Event 1 on 14 September 2017. The MMS-3 observations of (a) magnetic field perturbations in the two perpendicular directions, $\delta B_{\perp x}$ and $\delta B_{\perp y}$, (b) power spectrum of $\delta B_{\perp y}$,

This article is protected by copyright. All rights reserved.

(c) electric field perturbations in the two perpendicular directions, $\delta E_{\perp x}$ and $\delta E_{\perp y}$, (d) power spectrum of $\delta E_{\perp x}$, (e) electric field perturbations in the parallel direction, (f) power spectrum of parallel Poynting flux, and (g) the downward (red) and upward (blue) Poynting flux within the CDPS. Medium values of (h) PSD of $\delta E_{\perp x}$ and $\delta B_{\perp y}$ and (i) ratio of $\delta E_{\perp x}/\delta B_{\perp y}/V_A$ within 01:30-02:00 UT. The red line in (i) is the KAW dispersion.

Author Manuscript

This article is protected by copyright. All rights reserved.

Author Manuscript

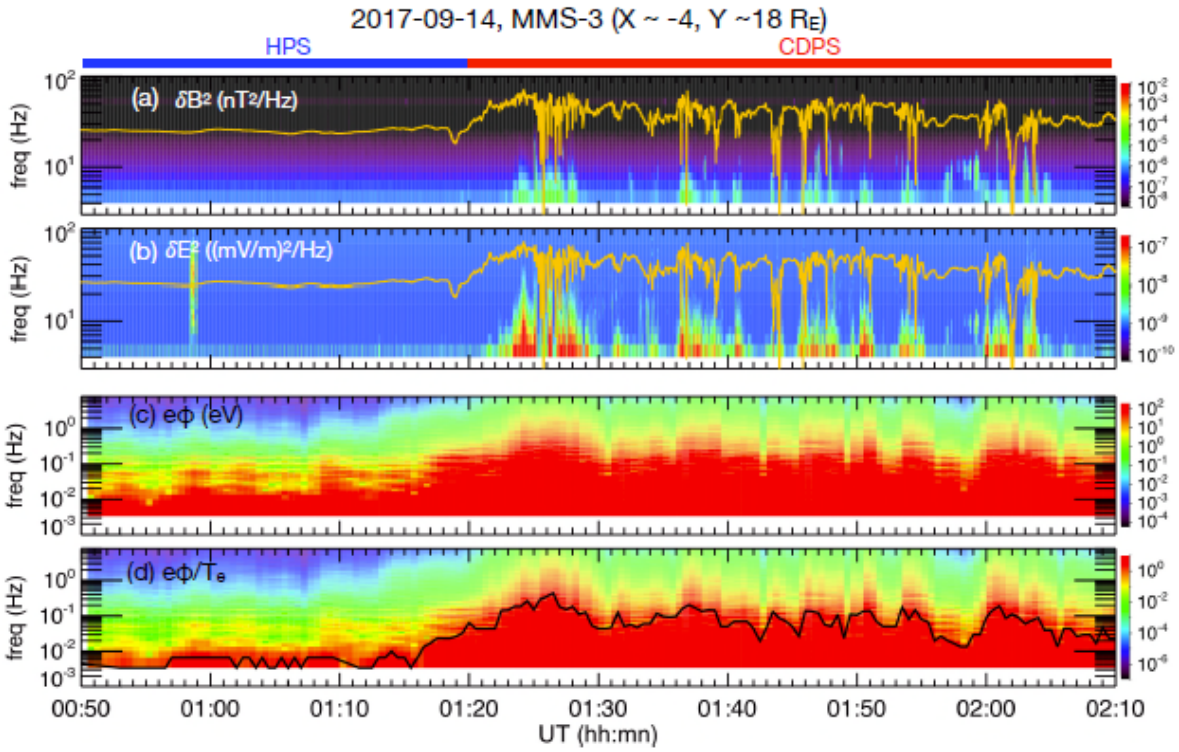

Figure 5. Event 1 on 14 September 2017. The MMS-3 observations of power spectrum of (a) δB and (b) δE. The yellow curves indicate the electron gyro frequencies. Computed power spectrum of (c) eΦ and (d) eΦ/T_e. The black line in (d) indicates $e\Phi/T_e = 1$.

This article is protected by copyright. All rights reserved.

Author Manuscript

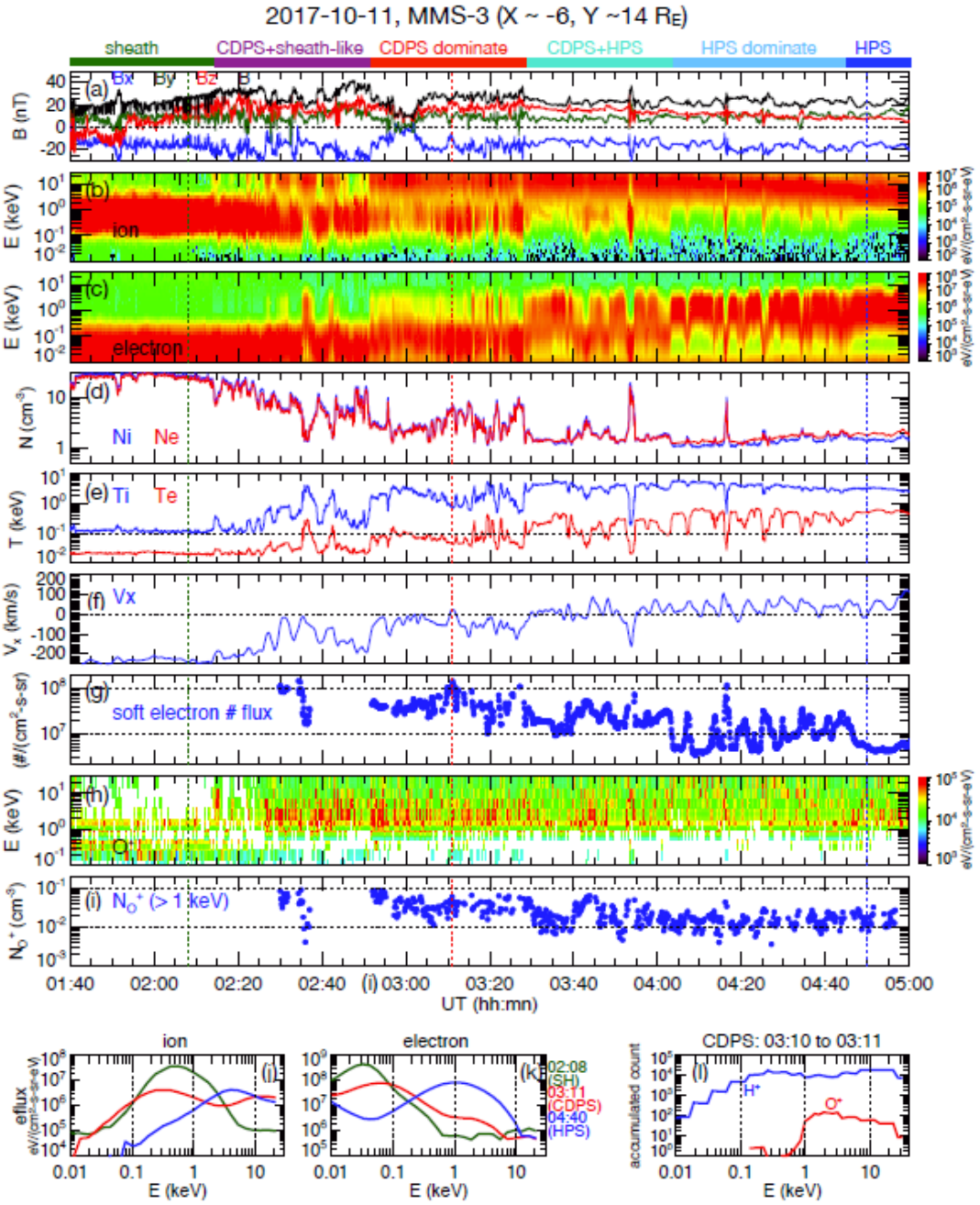

Figure 6. Event 2 on 11 October 2017. The MMS-3 observations of (a) magnetic fields, (b) ion and (c) electron energy fluxes, (d) ion and electron number densities, (e) ion and electron temperatures, (f) ion bulk flows in the X_{GSM} direction, (g) electron number fluxes integrated from

This article is protected by copyright. All rights reserved.

30 to 100 eV, (h) O^+ energy fluxes, and (i) the O^+ densities integrated over energies above 1 keV. Energy spectrum of (j) ion and (k) electron energy fluxes at three different times indicated by the vertical dotted lines in Figures 6a to 6i. (l) The accumulated H^+ (blue curves) and O^+ (red curves) counts within the 2-min interval indicated on the top of the plot.

Author Manuscript

This article is protected by copyright. All rights reserved.

Author Manuscript

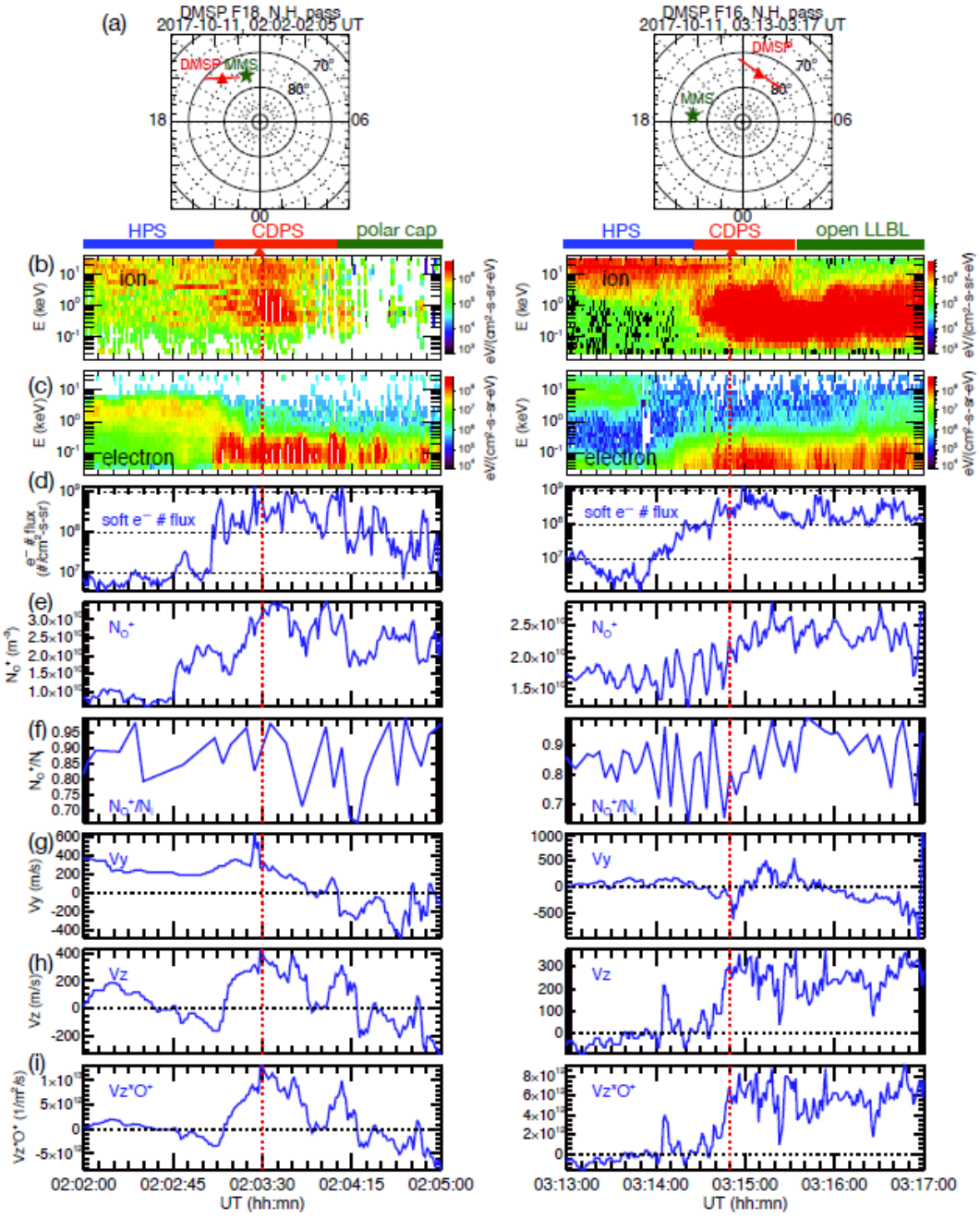

Figure 7. DMSP observations during event 2 on 11 October 2017 from 02:02 to 02:02 UT observed by F-18 and from 03:13 to 03:17 UT observed by F-16. (a) The red line indicates the

This article is protected by copyright. All rights reserved.

DMSP trajectory (the red triangle indicates the location corresponding to the time indicated by the vertical dotted lines in Figures 7b-7i.). The green star indicates the footprint of the MMS spacecraft. Temporal profiles of (b) ion and (c) electron energy fluxes, (d) electron number fluxes integrated over 30 to 100 eV, (e) the O^+ densities, (f) O^+/ion density ratios, (g) sunward flows, (h) upward flows, and (i) the O^+ upward fluxes.

Author Manuscript

This article is protected by copyright. All rights reserved.

Author Manuscript

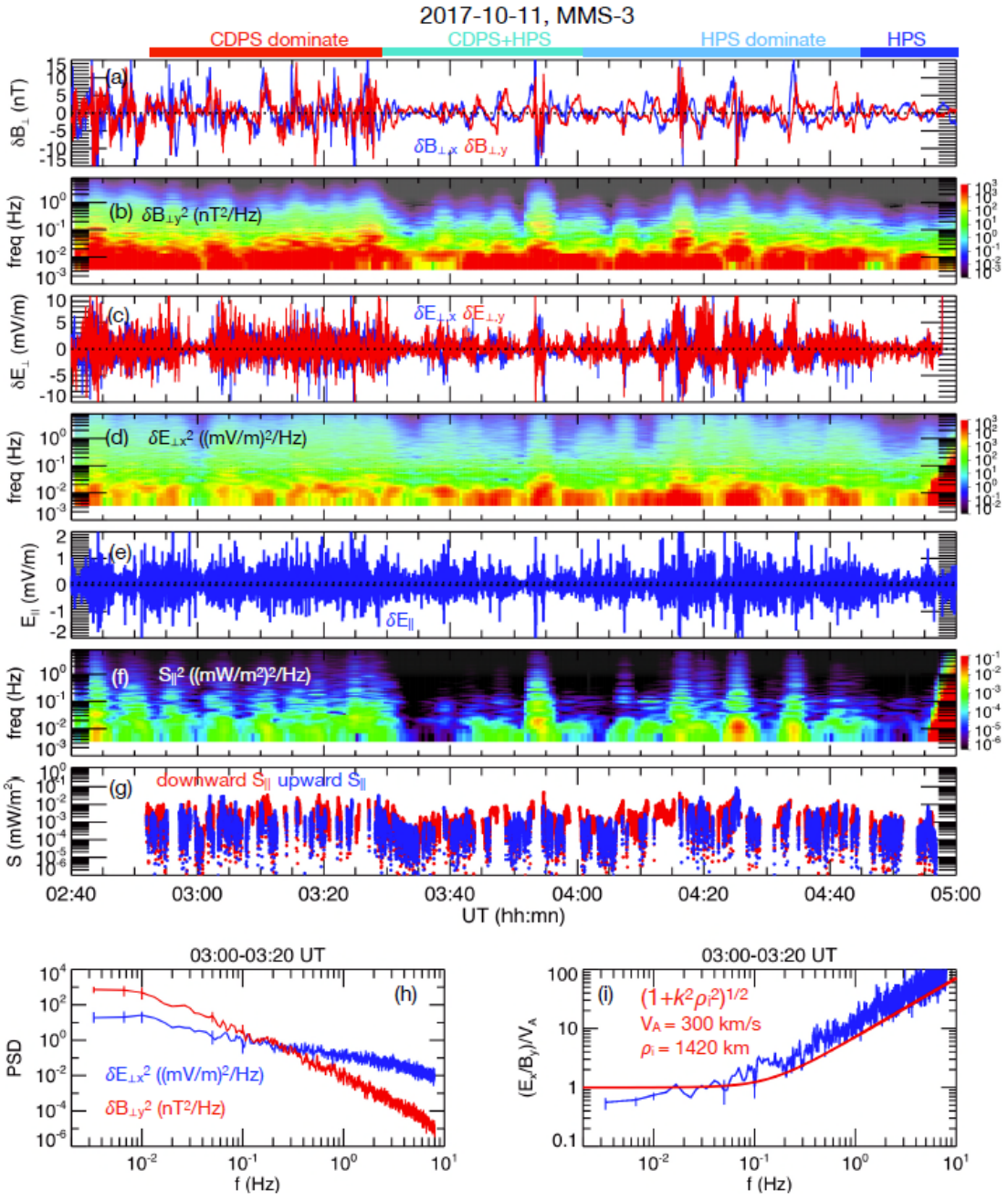

Figure 8. Event 2 on 11 October 2017. The MMS-3 observations of (a) magnetic field perturbations in the two perpendicular directions, $\delta B_{\perp x}$ and $\delta B_{\perp y}$, (b) power spectrum of $\delta B_{\perp y}$, (c) electric field perturbations in the two perpendicular directions, $\delta E_{\perp x}$ and $\delta E_{\perp y}$, (d) power

This article is protected by copyright. All rights reserved.

spectrum of $\delta E_{\perp x}$, (e) electric field perturbations in the parallel direction, (f) power spectrum of parallel Poynting flux, and (g) the downward (red) and upward (blue) Poynting flux within the CDPS. Medium values of (h) PSD of $\delta E_{\perp x}$ and $\delta B_{\perp y}$ and (i) ratio of $\delta E_{\perp x}/\delta B_{\perp y}/V_A$ within 03:00-03:20 UT. The red line in (i) is the KAW dispersion.

Author Manuscript

This article is protected by copyright. All rights reserved.

Author Manuscript

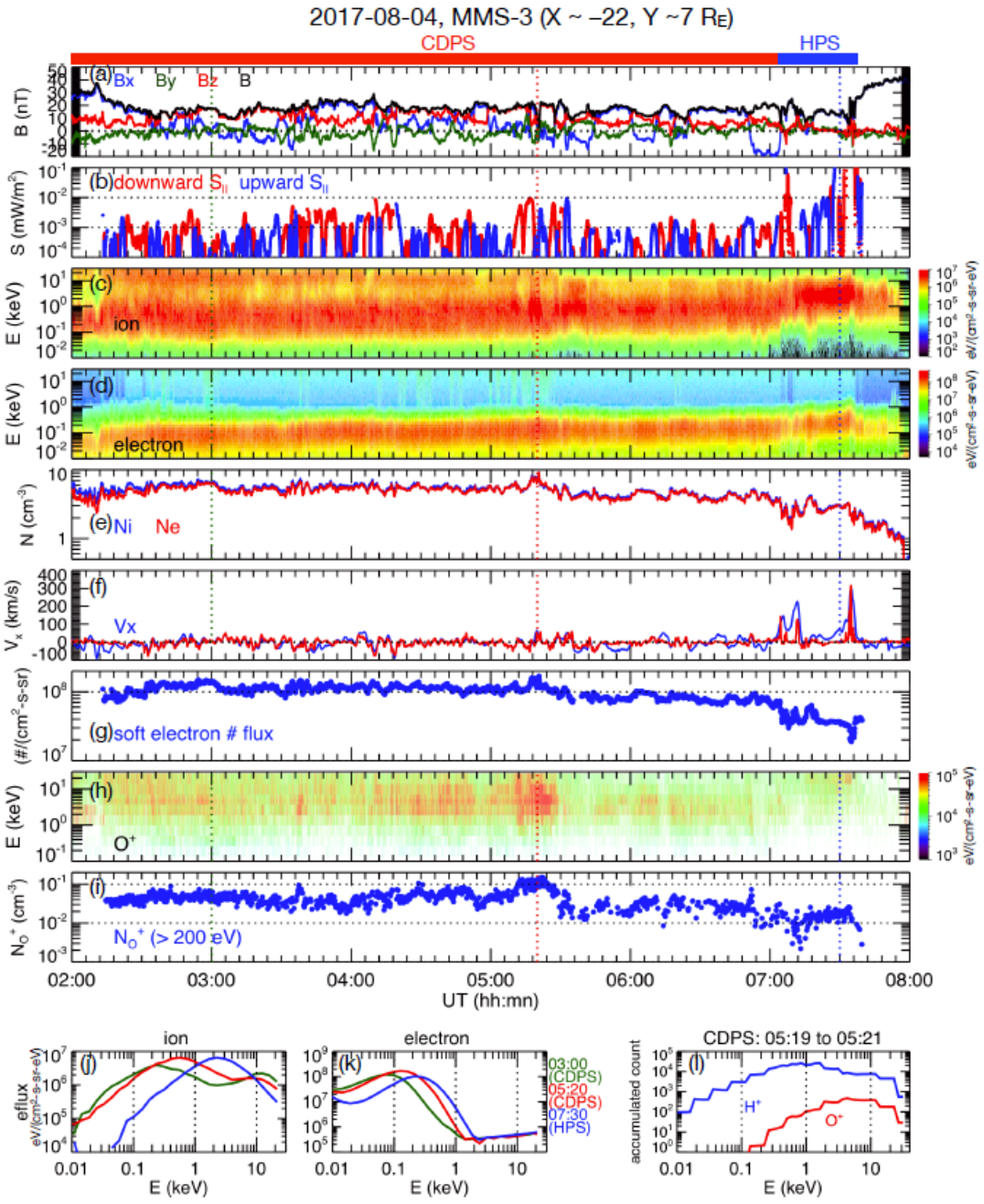

Figure 9. Event 3 on 04 August 2017. The MMS-3 observations of (a) magnetic fields, (b) the downward (red) and upward (blue) Poynting flux within the CDPS, (c) ion and (d) electron

This article is protected by copyright. All rights reserved.

energy fluxes, (e) ion and electron number densities, (f) ion bulk flows in the X_{GSM} direction, (g) electron number fluxes integrated from 30 to 100 eV, (h) O^+ energy fluxes, and (i) the O^+ densities integrated over energies above 1 keV. Energy spectrum of (j) ion and (k) electron energy fluxes at three different times indicated by the vertical dotted lines in Figures 10a to 10i. (l) The accumulated H^+ (blue curves) and O^+ (red curves) counts within the 2-min interval indicated on the top of the plot.

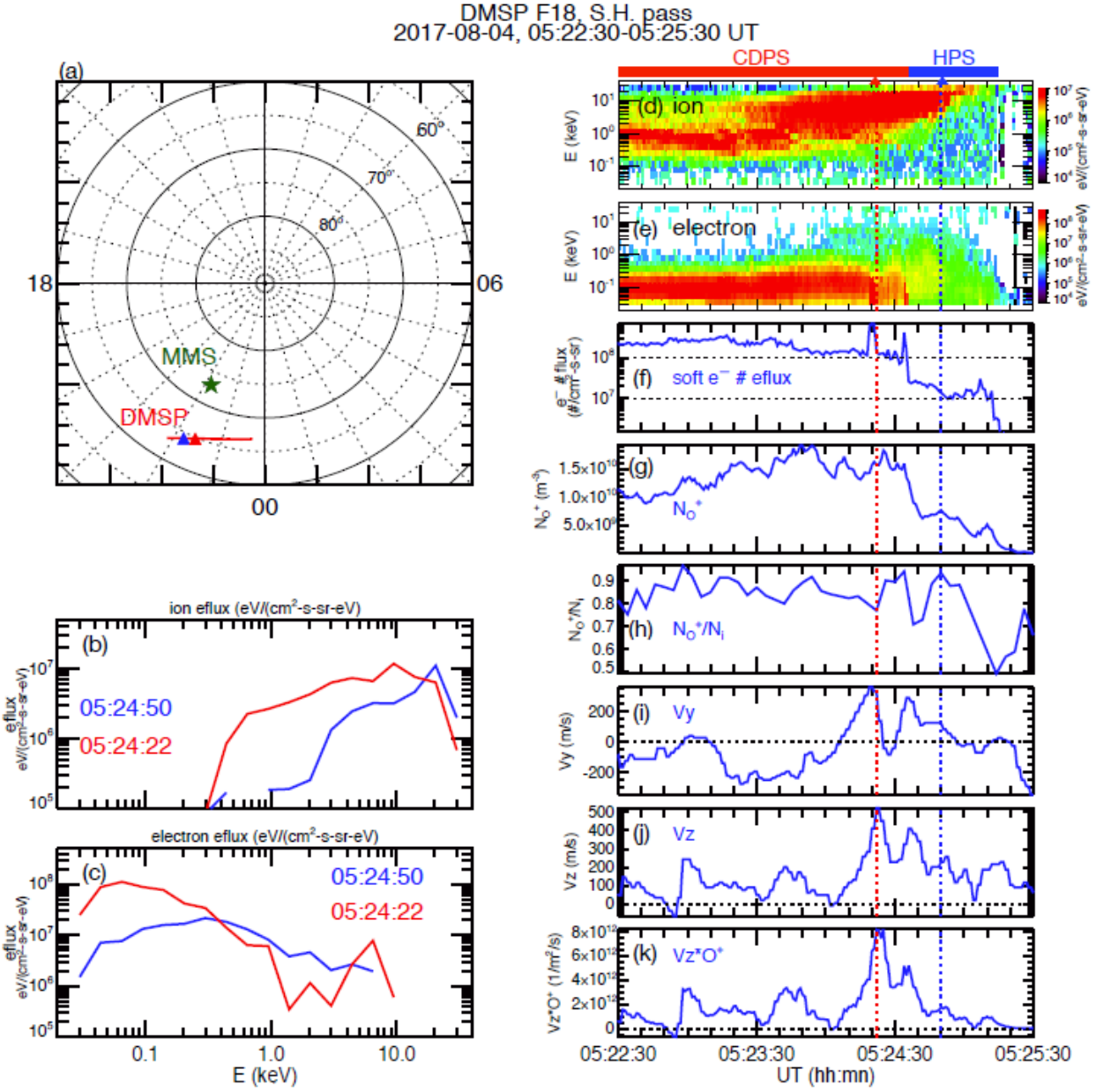

Author Manuscript

This article is protected by copyright. All rights reserved.

Figure 10. DMSP F-18 observations from 05:22:30 to 05:25:30 UT on 04 August 2017 for event 3. (a) The red line indicates the DMSP trajectory (the red and blue triangles indicate the location corresponding to the two different times indicated by the vertical dotted lines in Figures 10d-10k.). The green star indicates the footprint of the MMS spacecraft. Energy spectrum of (b) ion and (c) electron energy fluxes at the two different times. Temporal profiles of (d) ion and (e) electron energy fluxes, (f) electron number fluxes integrated over 30 to 100 eV, (g) the O^+ densities, (h) O^+/ion density ratios, (i) sunward flows, (j) upward flows, and (k) the O^+ upward fluxes.

Author Manuscript

This article is protected by copyright. All rights reserved.

Author Manuscript

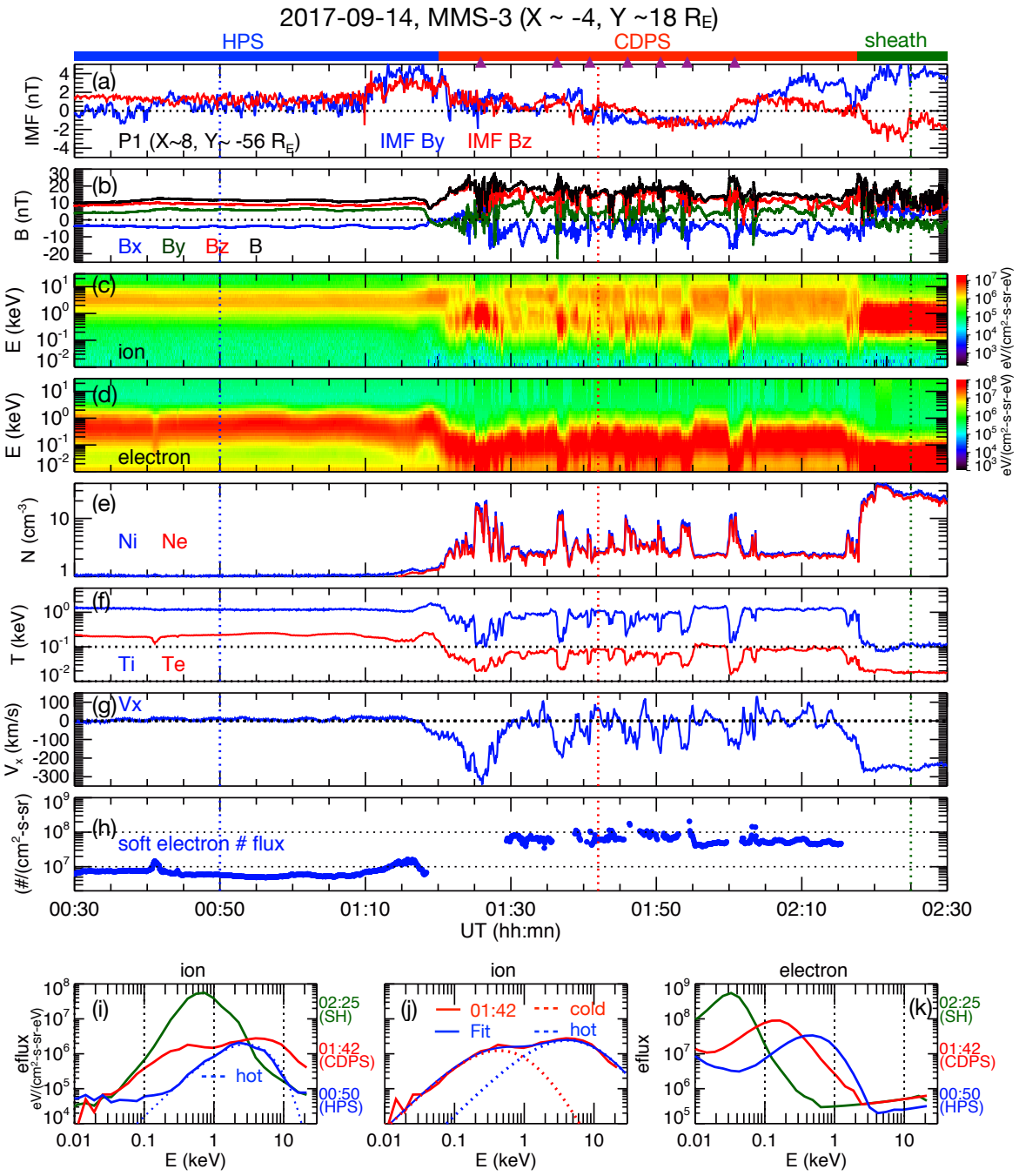

This article is protected by copyright. All rights reserved.

Author Manuscript

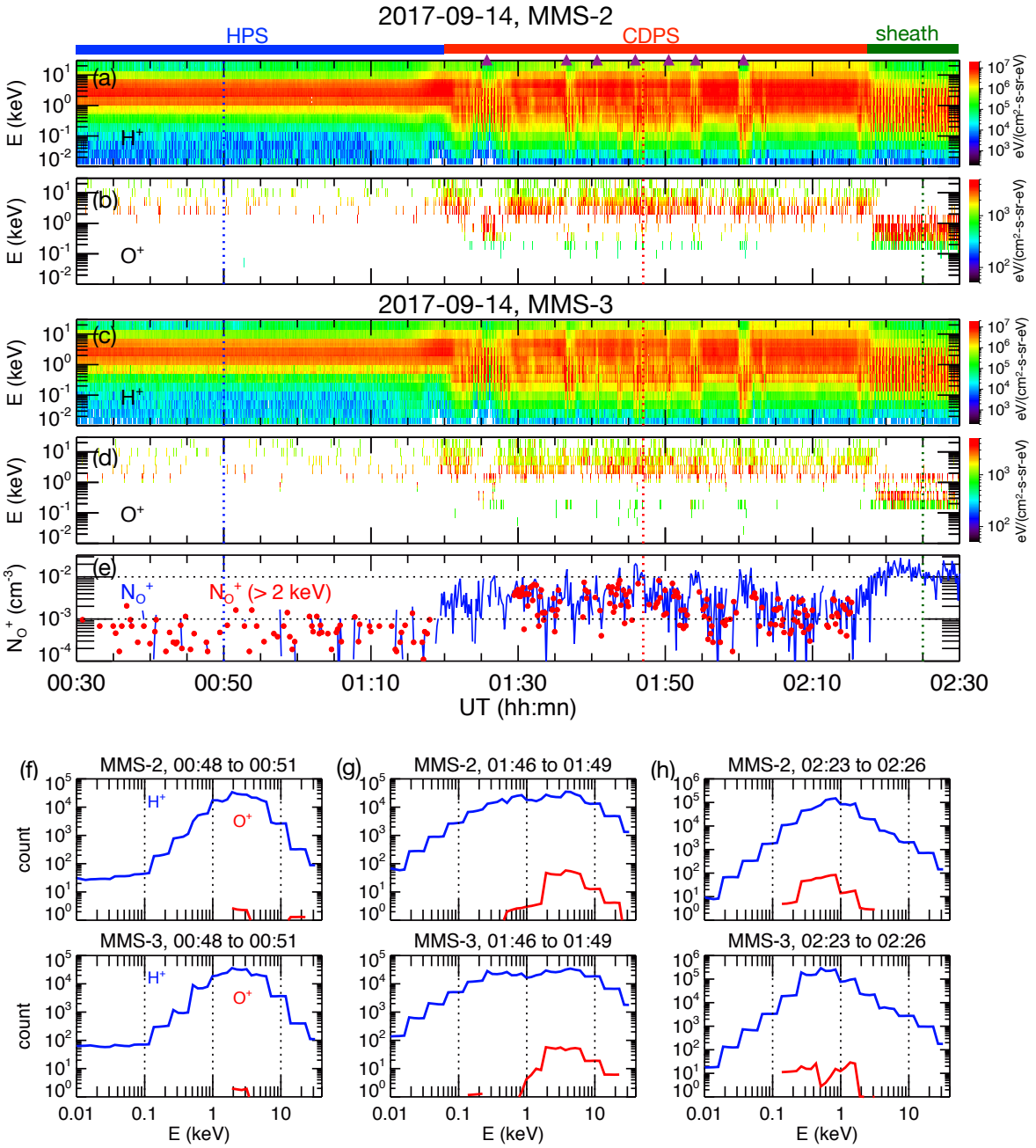

This article is protected by copyright. All rights reserved.

Author Manuscript

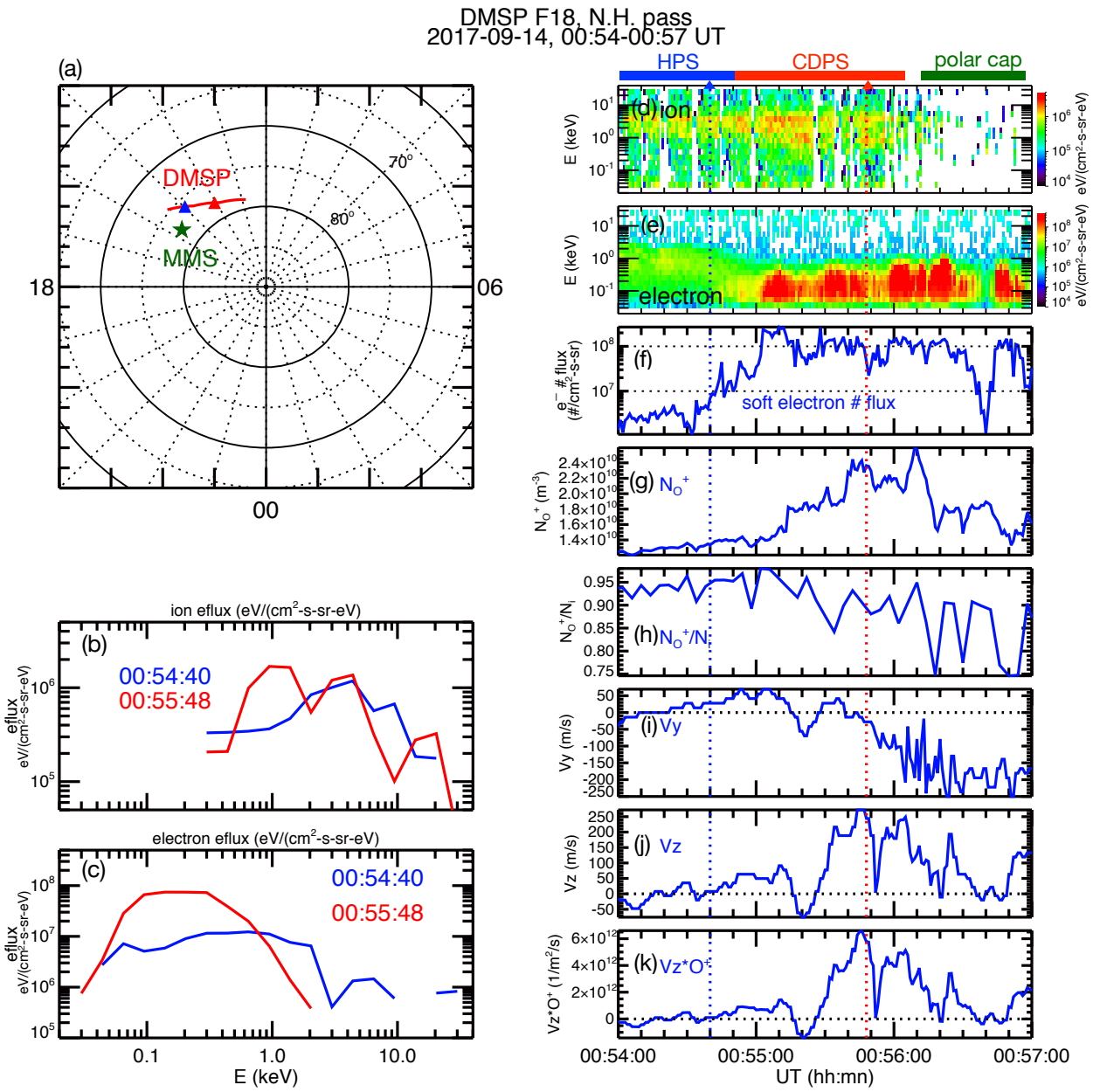

This article is protected by copyright. All rights reserved.

Author Manuscript

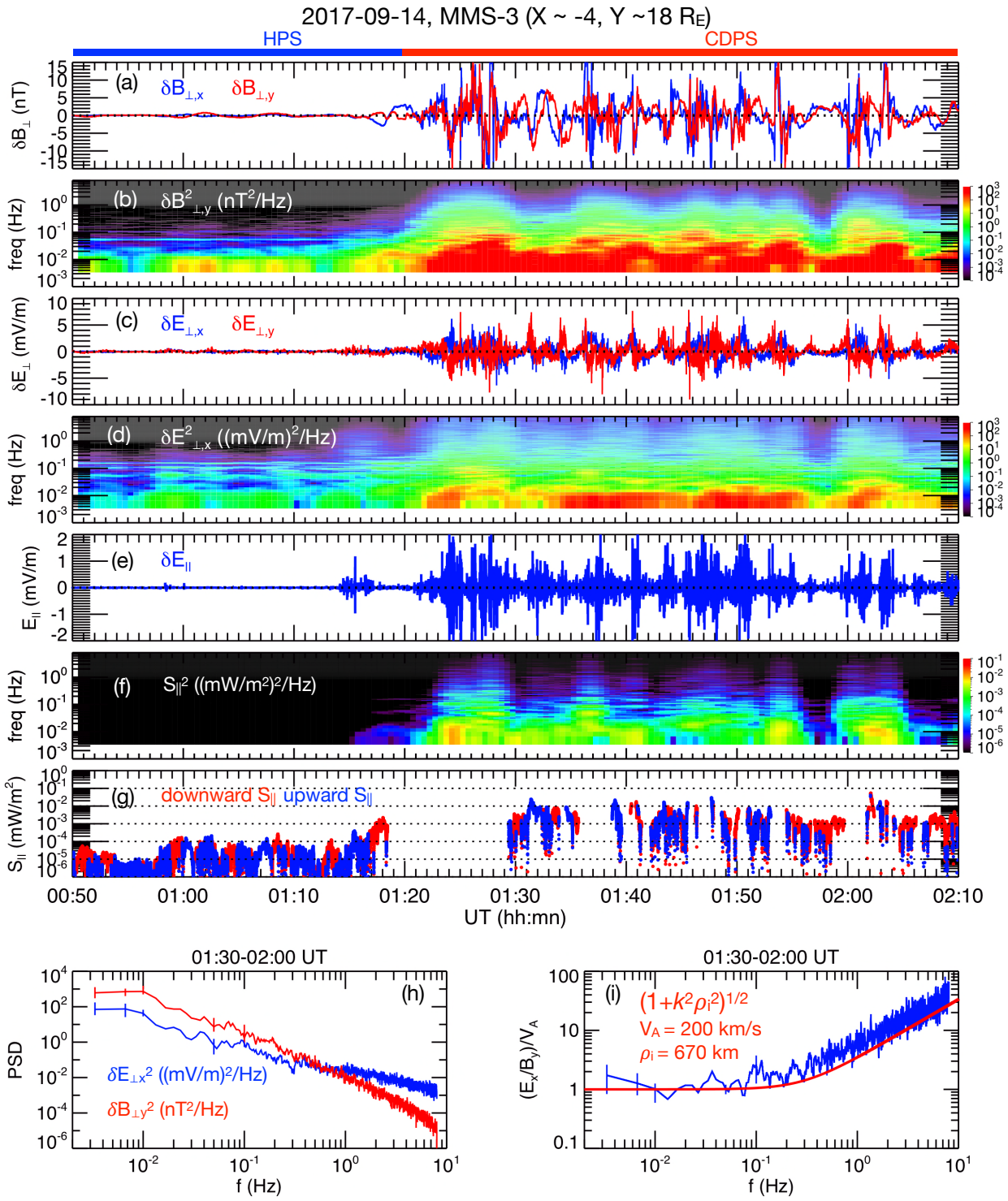

This article is protected by copyright. All rights reserved.

Author Manuscript

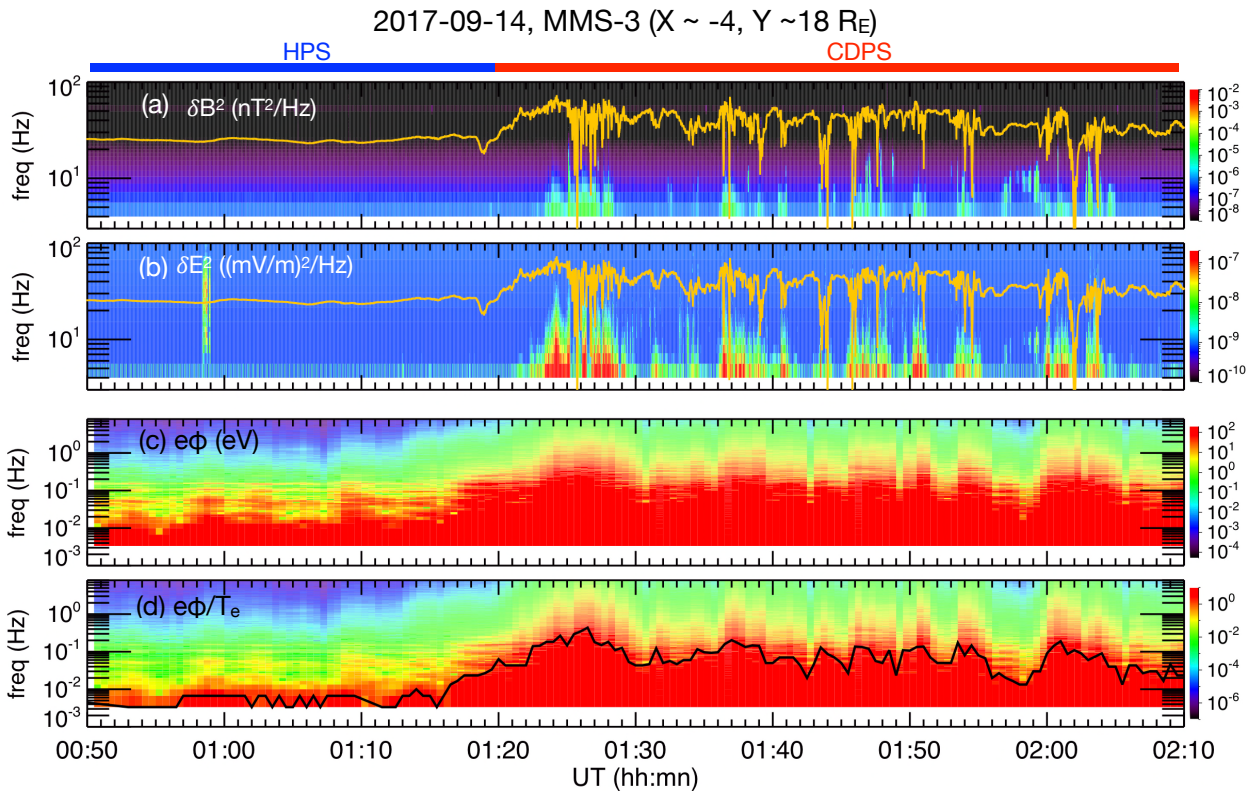

This article is protected by copyright. All rights reserved.

Author Manuscript

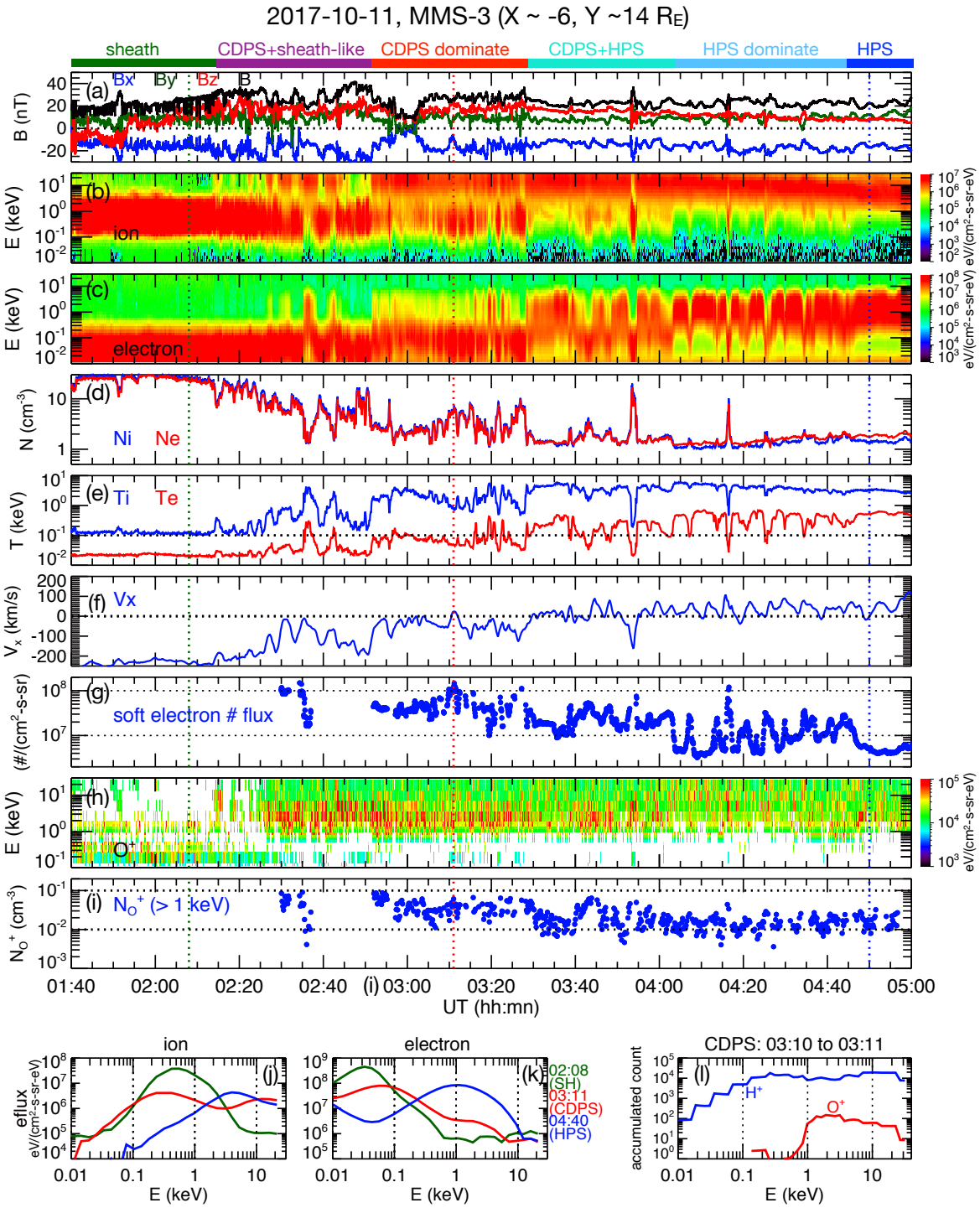

This article is protected by copyright. All rights reserved.

Author Manuscript

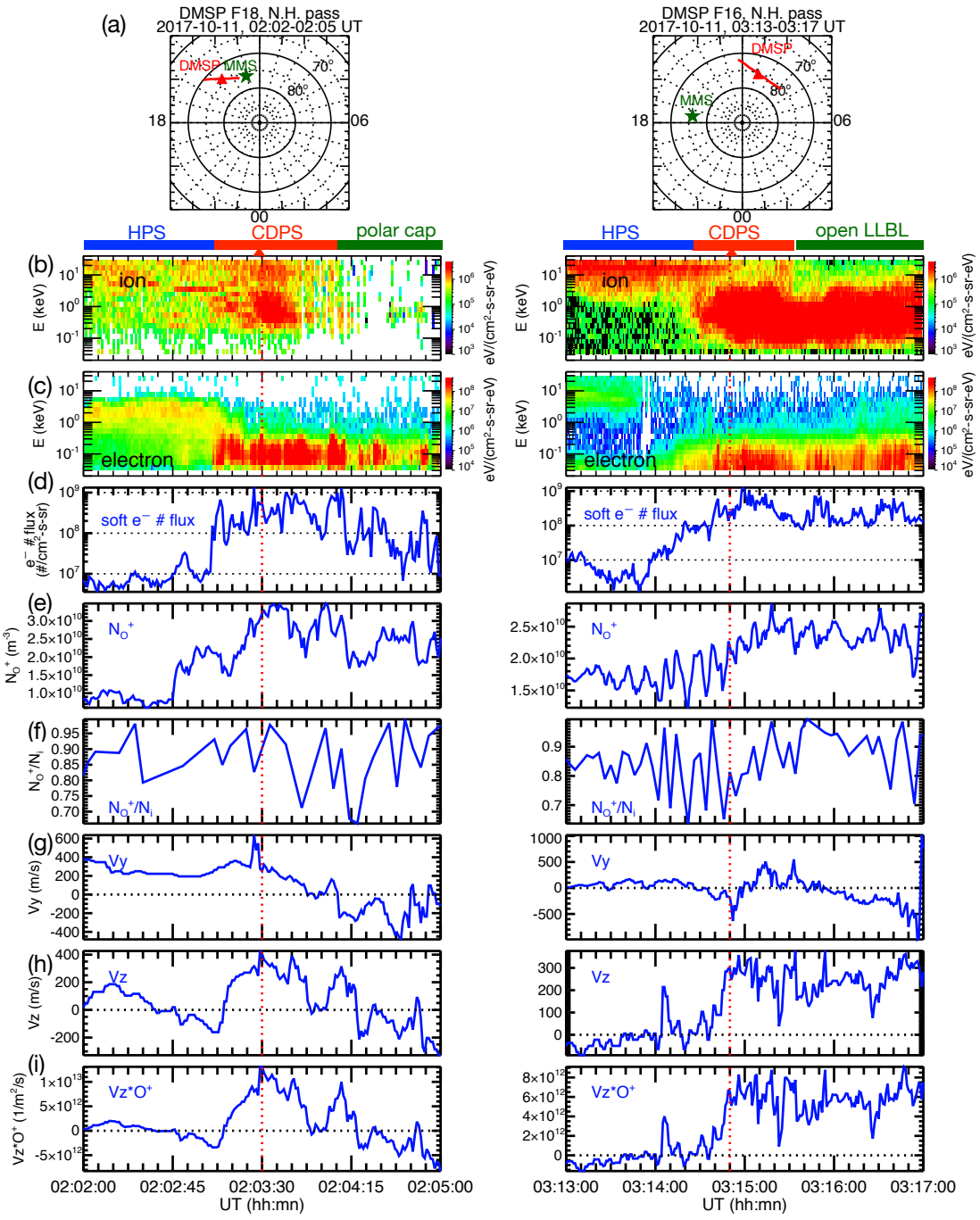

This article is protected by copyright. All rights reserved.

Author Manuscript

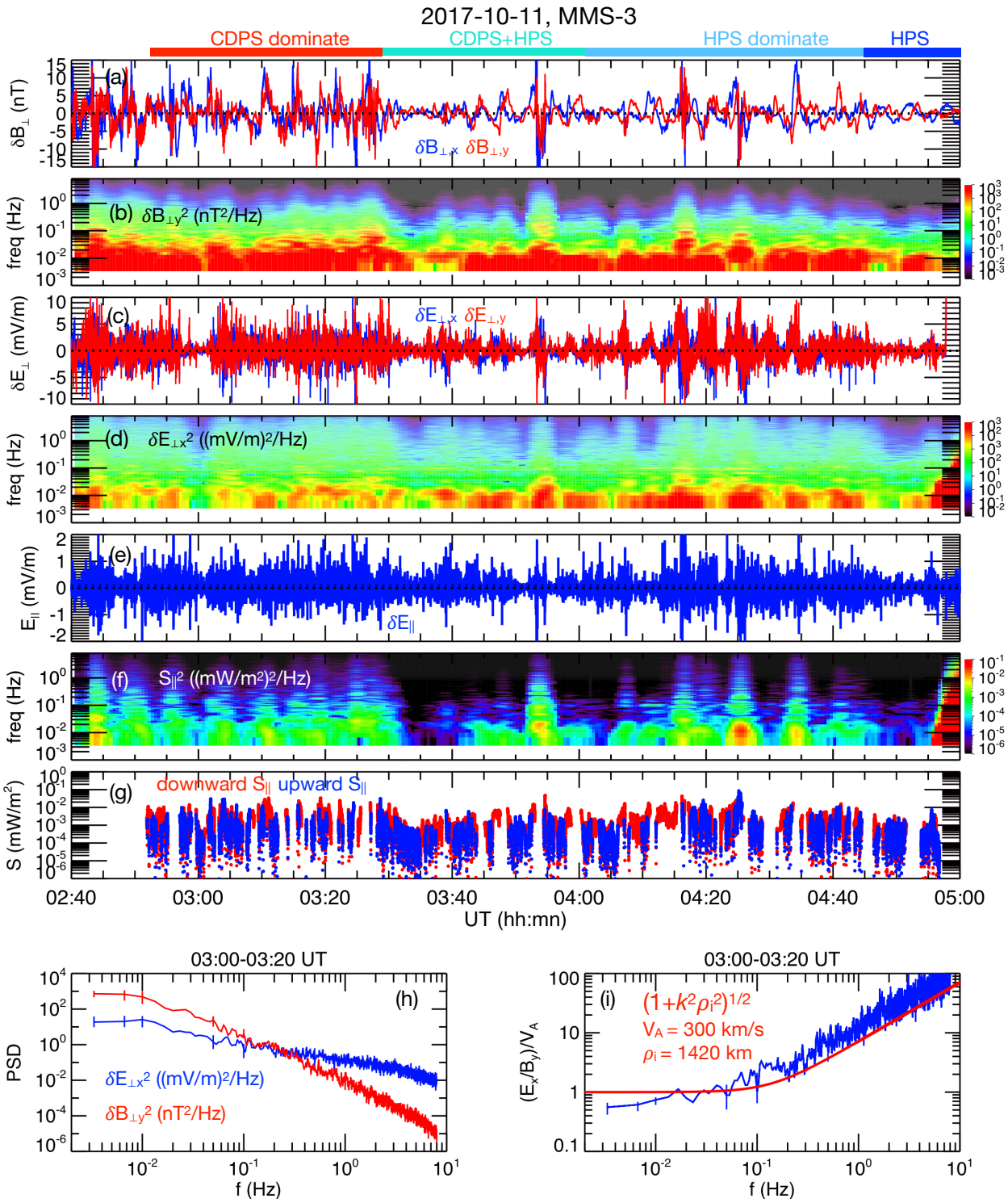

This article is protected by copyright. All rights reserved.

Author Manuscript

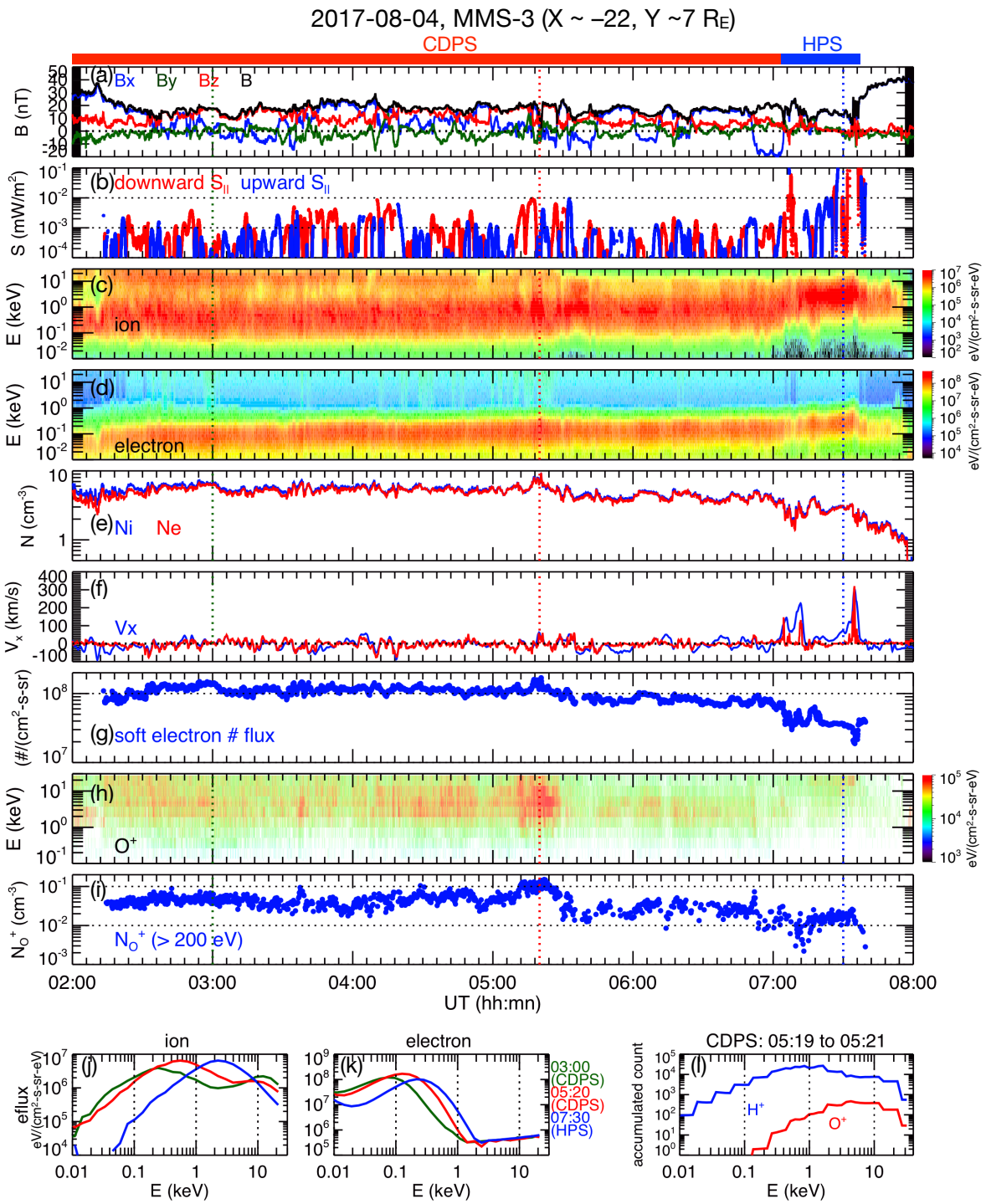

This article is protected by copyright. All rights reserved.

Author Manuscript

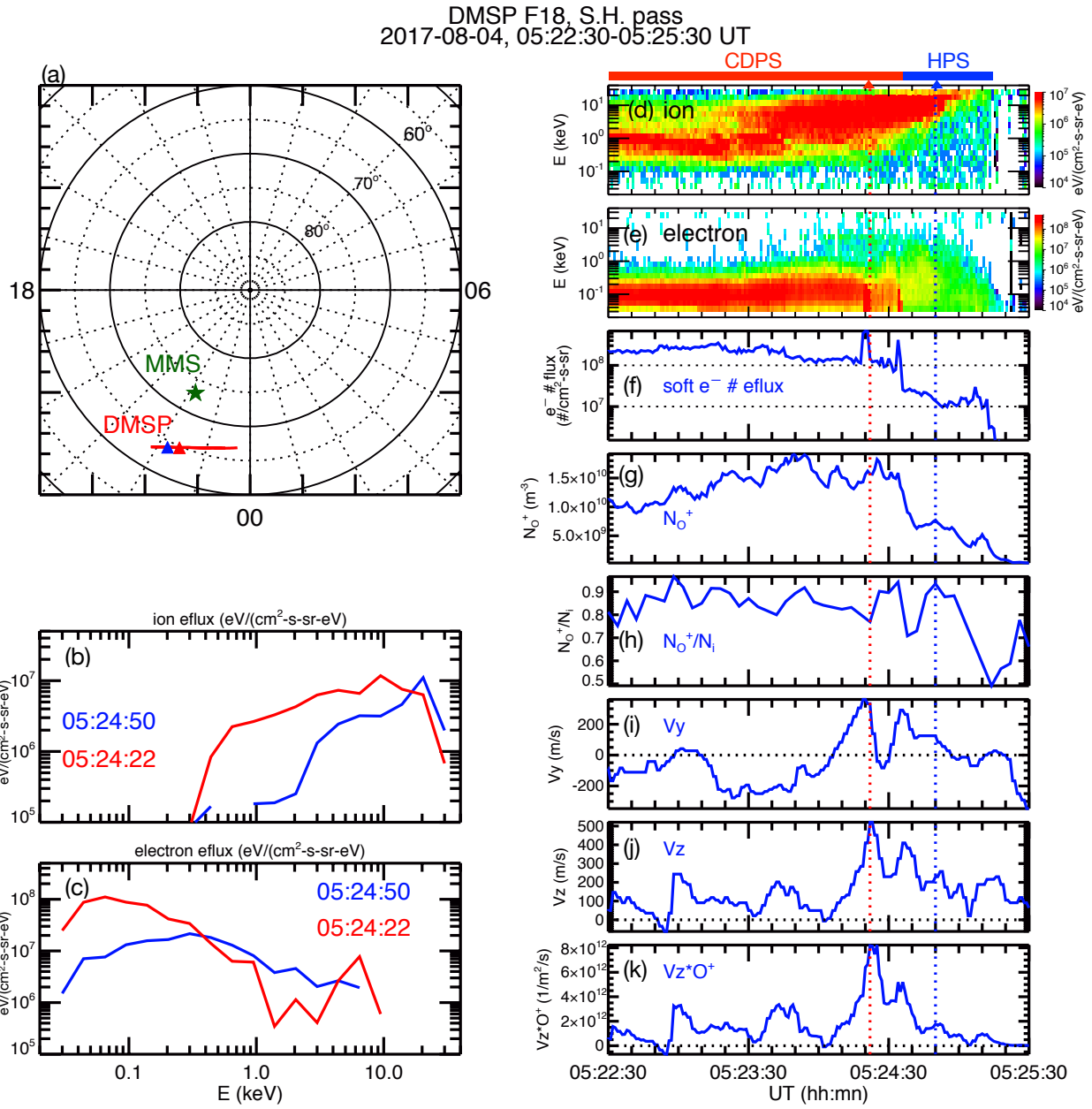

This article is protected by copyright. All rights reserved.